UNIVERSITA' DEGLI STUDI DI PADOVA

Department of Industrial Engineering

Master of Science in Aerospace Engineering

Modelling of supersonic turbulent boundary layers over cubical roughness

Thesis advisor
Dott. Cogo Michele

Thesis co-advisor
Prof. Picano Francesco

Candidate: **Depieri Davide**
Matriculation number: **2078173**

Academic year 2024/2025

Abstract

Understanding the behaviour of compressible fluids over rough surfaces is fundamental in many aerospace applications, especially those regarding atmospheric reentry, propulsion systems, missiles and aircraft. Every surface shows a rough texture, even if it appears smooth, and it is important to distinguish the cases where the topography is relevant or not in the evolution of the fluid dynamics. The influence of roughness is well known and theorised in the incompressible regime, and this knowledge lays the foundations for further elaboration in the compressible field; here, in fact, the thermodynamic effects, such as density and viscosity variations, become substantial. On top of that, shock waves and expansion waves are typical phenomena that may come into play. For these reasons, predicting drag and heat transfer in boundary layers is a rather difficult task. Re-entry vehicles are covered with ablative shields that undergo pyrolysis when invested by an extremely hot gas. This process generates particular roughness patterns that interact with the external flow with a consequent change in the performance of the vehicle. The purpose of this thesis is to develop a wall model that is effective in describing the velocity and temperature profiles in the boundary layer, given the values at a certain distance from the wall (called the matching location) and information about the roughness topography. The main focus will be on a supersonic, zero-pressure-gradient, turbulent boundary layer at a free-stream Mach number of $M_\infty = 2$ over cubical-shaped elements. (DNS data for comparison are provided by Cogo et al., 2025). The model presented here is an extension of the one developed by Yang et al., 2016. The present work extends and adjusts the model for supersonic applications based on the fact that, in the near-wall region, the compressibility effects are negligible due to the slowing of the flow. Outwards the roughness crest, instead, the velocity profile has a logarithmic behaviour. In order to take into account density variations, a compressible transformation (Van Driest, 1951) is implemented in the logarithmic region, while the temperature profile is obtained from the Reynolds analogy proposed by Zhang et al., 2014. The results agree with the simulation data for both the adiabatic and isothermal wall. In the future, it could be interesting to analyse more complex and realistic geometries and compare the model with simulations at hypersonic speeds. In addition, the model needs to be elaborated and tested in full scale simulation of re-entry vehicles.

Contents

1. Introduction

1.1 Scientific background

Turbulent flows represent the majority of cases in nature; from the smoke coming out of a chimney to the movement of water down a waterfall, fluid flux is irregular, unsteady, and unpredictable. This is due to the fact that the viscous forces are not strong enough to contrast the inertial ones. Turbulence also affects anthropic activities, such as the flow of water near the hulls of ships, the airflow around the wings and fuselages of planes, same for car bodies surfaces, and the wind passing through the houses and skyscrapers of our cities. It is of great importance to predict how much drag an object produces while moving in a fluid medium, especially for how this reflects on economic aspects. Unfortunately, predicting the skin friction of a surface is a difficult task, particularly if the flow is highly unpredictable and the skin presents a rough texture. These issues amplify when the object proceeds at supersonic or even hypersonic speeds because the compressible nature of the fluid starts to come into play. This work will focus mainly on the latter case, which finds application in predicting drag and heat transfer during the reentry phase of space vehicles or the descending phase of space probes on planets with an atmosphere like Mars. This type of spacecraft is often covered with special materials that undergo pyrolysis to absorb most of the thermal flux and protect the delicate structure underneath. There are two types of thermal protection system (TPS), ablative or tiled. The first involves heat absorption through the loss of material. There are some types of plastics reinforced with organic fibres that when exposed to a high-temperature environment undergo pyrolysis. This process generates hot gases that take away the heat from the layer by blowing the boundary layer away from the surface. The surface ablates with a non-uniform recession rate, resulting in regular or irregular distributed roughness patterns, depending on the type of material. Because of its method of operation, this type of TPS is not reusable. The tiled type, on the other hand, is reusable. It consists in a series of ceramic or carbon tiles that can have a square, diamond or hexagonal shape, and the presence of space between the tiles is what forms a structured roughness pattern on the surface. These textures can alter the dynamics of the external flow with a consequent change of the aerodynamic performance and the heat transfer. The analysis of the hypersonic flow around blunt bodies, which can be representative of a capsule re-entering a planetary atmosphere, is a state-of-the-art problem that has always been strongly linked to the experimental data. A better understanding of how thermal and mechanical loads apply to a spacecraft covered with a realistic and complex rough shield will lead to the realisation of wall-models that can be used to predict the behaviour of a capsule in a real-case scenario. The goal of many researchers is to understand the dynamics of an entry, descent and landing phase (EDL) of a Martian probe, since it represents the next step in space exploration.

In general, the level of the heating is dependent on:

- vehicle shape: re-entry vehicles are blunt shaped, with a high curvature radius to dissipate more heat;
- entry speed and flight trajectory: as re-entry speed increases, both convective

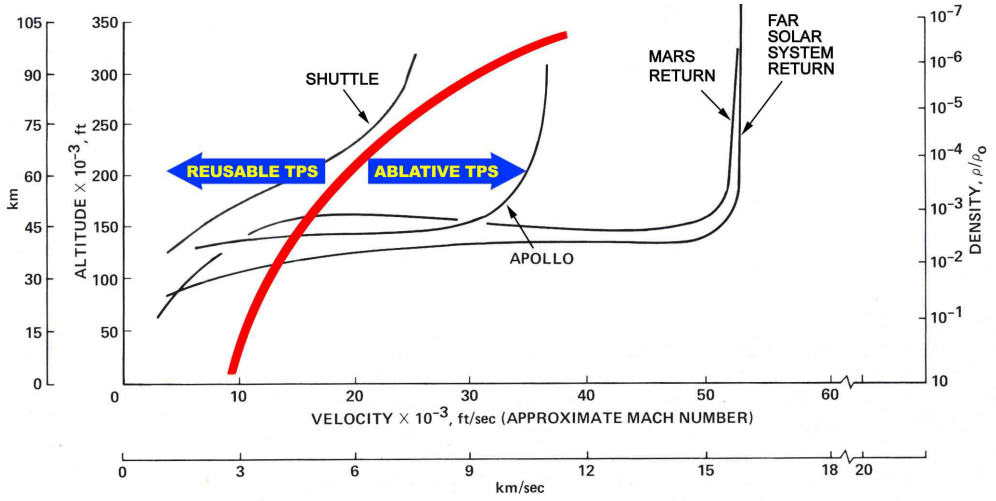

Figure 1: Application of the two types of TPS (re-usable and ablative) based on mission profile (credit: NASA).

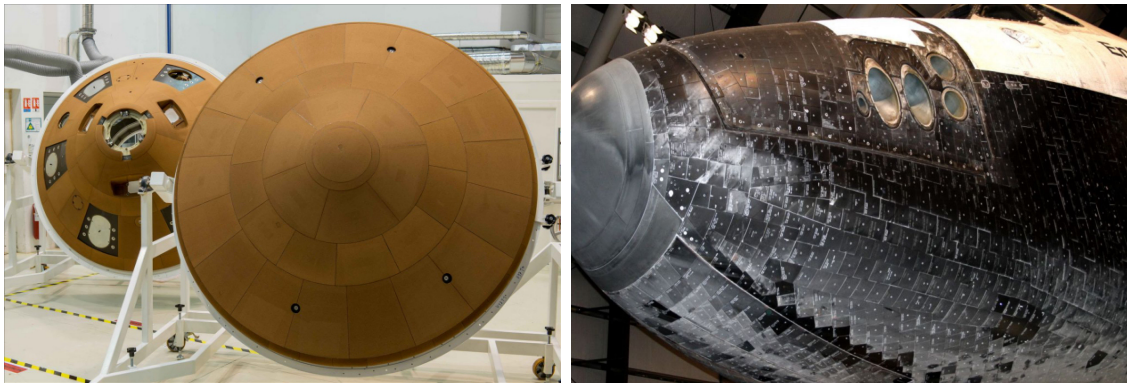

(a) (b)

Figure 2: (a) Example of ablative TPS on the Schiaparelli heat shield (credit: ESA). (b) Example of a tiled TPS on the space shuttle (credit: NASA).

and radiation heating increase;

- atmospheric composition: Earth and Mars have completely different atmosphere in terms of chemical composition, density and temperature stratification;

- TPS material composition and surface properties;

Vehicles returning from Mars missions would have entry velocities of 11 to 15 km/s. Flight velocities of this magnitude are associated with high-temperature chemical reactions that significantly affect airflow around the spacecraft (at entry speeds greater than 11 km/s temperatures greater than 11,000 K are encountered in the shock layer). At altitudes above 80 km the density of the atmosphere is so low that the average distance an air molecule travels between successive collisions with other air molecules is large compared to the size of the object considered. This condition is referred to as the free molecular flow regime in contrast to the

continuum flow regime at lower altitudes. Atmospheric entry trajectories are shown as functions of altitude and velocity in figure 1. At high altitudes, free molecular flow effects are significant and continuum flow approximations are not valid. At low altitudes continuum subsonic, transonic, supersonic and hypersonic flows occur. At vehicle speeds below about 100 m/s, the flow can be considered incompressible (air density is assumed constant). For each flow regime, it is necessary to consider the flow field around the vehicle, the vehicle surface pressure distribution, and the heat transfer to or from the vehicle.

This topic also covers many other fields of engineering. Some examples are erosion, corrosion, and deposition that compromise the performance of propulsion system components (such as turbine blades) and ice formation on aircraft aerodynamic surfaces.

(a) (b)

Figure 3: (a) Apollo and Orion ablative heat shields before and after testing (credit: NASA). (b) Example of a thermal protection roughness structures (image from Miller et al., 2024).

The main task of many researchers is to simulate more complex and realistic geometries at high speed. For example, diamond-shaped grooves are a particular pattern that develops in ablative surface (the pattern is also known as cross-hatch).

More in general, roughness is the result of every manufacturing process. Although the available technologies are advanced in reaching a high level of polishing and finishing, these operations have a considerable cost and require a certain amount of time; therefore, industries will avoid them if they are not profitable.

1.2 Bibliographic research

Nominally, every surface shows at least some rough texture, but the flow that runs next to it could not perceive it. In this case, we consider the surface to be hydraulically smooth, but in other cases, the asperities could influence the dynamics of the main flow. Practically speaking, a surface cannot be considered hydraulically smooth if its topographical structure alters and disrupts the smallest eddies next to the wall, hence affecting momentum, heat, and mass exchange. For example, all surfaces with topographical features larger than $10\mu m$ on the hulls of ships and

aircraft or $1\mu m$ on the blades of gas turbines cannot be considered smooth, but must be treated as rough surfaces (Chung et al., 2021).

Hagen (1854) and Darcy (1857) were the first to study turbulent flows over rough walls mainly because they were concerned with pressure losses in water conduits. Important contributions came later, thanks to Nikuradse (1933) and Moody (1944), who computed his famous skin friction diagram for pipes.

Basically, flows over rough surfaces have been studied for more than a century, but most of the studies collected so far focus on the incompressible regime, which is well documented from both the experimental and numerical point of view. The fundamental problem is to predict performance-critical quantities such as drag and heat transfer, but because each roughness topography affects flow differently, routine predictions currently remain insufficiently reliable, with uncertainties costing billions of dollars per year. For these reasons, this topic continues to be an active area of research. The challenge in research has been the large number of relevant topographies and the costs associated with testing each topography, but these barriers have been reduced since the publication of Jiménez, 2004, who first discussed some core features on how rough walls can be modelled without a detailed calculation of the flow around the roughness elements themselves. In addition, the advances of high-fidelity simulations and rapid prototyping technologies as viable tools have allowed investigations of a growing set of roughness topographies with unprecedented levels of detail and accuracy. Researchers refer to the equivalent sand grain height k_s to compare the effects of different topographies on flow dynamics. Basically k_s is the characteristic length that the sand grain roughness, originally studied by Nikuradse, must have in order to match the same drag as the surface of interest.

For what concerns compressible, turbulent flows over rough walls, the subject is much more complicated. The available literature lacks theoretical studies on the topic. For high-speed flows, many of the differences in the mean and turbulent statistical properties across smooth plate boundary layers have been explained, or at least correlated by including the thermodynamic property variations across the layer in the scaling. In summary, there is ample evidence to confirm the use of van Driest II theory (Van Driest, 1951) to correlate high-speed, zero-pressure gradient, smooth-wall mean velocity profiles with the low-speed database. However, supersonic flows are more complicated and often possess features that do not have incompressible counterparts. For example, supersonic flow over rough surfaces can generate shock and expansion waves that can interact with boundary layer turbulence all the way across the boundary layer. This is especially true at high Mach numbers and Reynolds numbers, where most of the boundary layer is supersonic. Hence, the presence of relatively small roughness elements could generate significant compressibility effects across the boundary layer (Bowersox, 2007). During the last years, there have been only a few experimental studies (Ekoto et al., 2008, Peltier et al., 2016 and B. D. Kocher et al., 2022) because the setups are very expensive, and even fewer numerical simulations (Modesti et al., 2022, Cogo et al., 2025) because they require a lot of computational resources.

Goddard Jr, 1959 made experiments at various Mach numbers (in a range between $M = 0.7 - 4.54$) to investigate the mean velocity profiles and the friction coefficient around a body of revolution. He demonstrated that when the Van Driest

transformation is applied, the profiles follow the same trend of the incompressible cases. Morkovin, 1962 stated that the variation of thermodynamic quantities across the boundary layer is related to the differences of the turbulent statistics between subsonic and supersonic smooth plates.

Latin et al., 2000 performed experiments at $M = 2.9$ on six different rough plates, and in some cases (when the roughness is of the k-type) they assisted to the development of shock waves and expansion waves whose intensity was proportional to the roughness height. In addition, these phenomena visibly altered the free-stream region.

Ekoto et al., 2008 examined the effects of two rough patterns (distributed square and diamond) on a supersonic turbulent boundary layer ($M = 2.86$). The square roughness induced weak waves, while the diamond one displayed far more visible phenomena with consequent distortion of the flow (fig. 4).

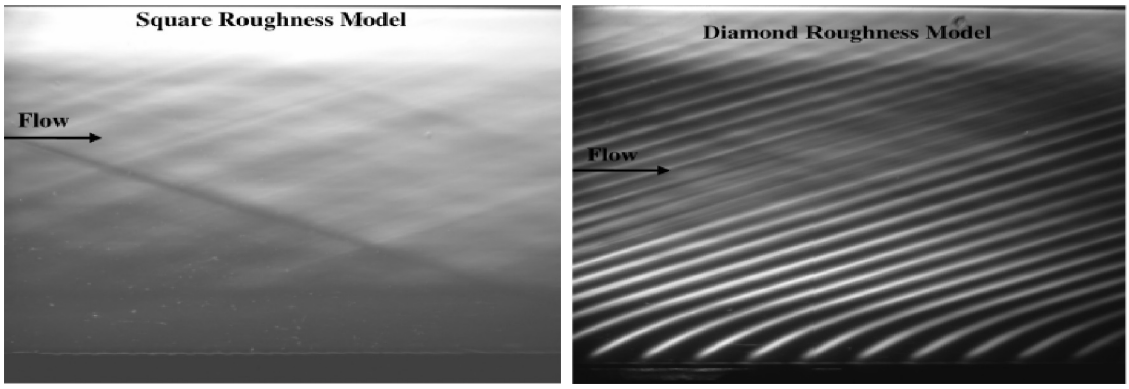

(a) (b)

Figure 4: Schlieren photographs for the Ekoto et al. experimental setup (Ekoto et al., 2008).

Peltier et al., 2016 carried out experiments to document the effects of cross-hatch (diamond) roughness on a $M = 4.9$ turbulent boundary layer; shock and expansion waves were observed at the leading and trailing edges of the diamond elements to prominently protrude into the boundary layer and free-stream respectively.

B. Kocher et al., 2022 investigated the effect due to surface roughness topologies in a Mach 2 boundary layer. Three roughness topologies were studied: a smooth plate as a reference, a uniformly distributed diamond roughness pattern, designed to be similar to the one of Peltier et al., 2016, and a third one characterised by a highly non-uniform topology used to reproduce a "realistic" roughness usually found in turbine blades affected by wear and/or damage from debris. The findings were consistent with previous researches. However an intriguing characteristic arose for the "realistic" roughness, with non-uniform mechanical distortions over the length of the test bed that were not ascribable to shock waves, but to Mach waves, with an angle of incidence of $30 \pm 1°$, similar to the Mach angle for a flow at $M = 2$.

Measurement of skin friction and heat transfer during an experiment is a difficult task because the setup can lead to uncertainties when capturing the characteristics of the flow close to the wall. Computational analysis represents a useful alternative to overcome these obstacles. However, even if the resolution required to capture the

properties of the flow near the wall is very high, the modern advances in computational technologies are promising to produce high-fidelity results in progressively lower times and costs.

Tyson et al., 2013 performed direct numerical simulations (DNS) to assess alterations in mean flow and turbulence properties of turbulent rough channel flows at different Mach numbers ($M = 0.3, 1.5, 3.0$). The roughness surfaces under inspection were 2D sinusoidal waves and the influence of other parameters such as the amplitude and the wavelength of those waves have also been investigated. In the $M = 3.0$ cases, shock waves occurred, leading to profound modifications in the turbulent statistics.

Modesti et al., 2022 executed DNS of a supersonic turbulent channel flow over cubical roughness elements in an attempt to represent the typical roughness patterns found in ablative shields of high-speed vehicles. They compared rough-wall flows across different Mach numbers, $M = [0.3 - 4]$, and found that, as in the incompressible flow regime, the mean velocity profile shows a downward shift with respect to the baseline smooth-wall cases. However, the magnitude of this velocity deficit is largely affected by the Mach number. Compressibility transformations are able to account for this effect, and the data showed very good agreement with the incompressible, fully rough asymptote. Velocity statistics present outer layer similarity with the equivalent smooth wall cases; however, this does not hold for the thermal field, which is substantially affected by the roughness, even in the channel core. This is a direct consequence of the quadratic temperature–velocity relationship, which is also valid for rough walls. Analysis of the heat transfer showed that the relative drag increase is always larger than the relative heat transfer enhancement; however, increasing the Mach number brings the data closer to the Reynolds analogy line due to the increasing relevance of the aerodynamic heating.

Finally, Cogo et al., 2025 performed DNS of a supersonic turbulent boundary layer at $M = 2$ over cubical roughness elements and evaluated the velocity and thermal statistics to confirm the influence that roughness has on both mean and fluctuating quantities. The model presented in this work uses data from Cogo et al., 2025 as a reference.

2. Scientific gap

2.1 Purpose of the study

The present thesis aims to develop a model that predicts the mean drag force per unit area (or shear stress) τ_w and the mean heat transfer $q_w = -\lambda \frac{\partial T}{\partial n}\big|_{wall}$ (where λ is the thermal conductivity of the gas and n is the wall-normal direction) exerted on a supersonic flow by a rough wall. The topographies of the surfaces under investigation are composed of aligned and staggered cubical elements. These patterns are very simple to analyse in terms of geometrical properties (for example, the roughness height and the solidity, which will be explained later) and they allow researchers to directly understand their effects on the dynamics of the boundary layer. Starting from a point at a certain distance from the wall, called matching location, the developed model is capable of determining the velocity and temperature profiles in the logarithmic layer (which will later explained in section 3.1.2), thanks to the knowledge of the roughness conformation. The logarithmic region is the most important zone of the boundary layer because it contains information about the drag and heat transfer exerted by the wall. Since the available literature mainly focuses on the incompressible regime, this work wants to extend the knowledge to supersonic applications by adopting compressible transformations and temperature-velocity profile relations. Currently, most of the studies revolves around adiabatic walls, in which the temperature gradient (and consequently the heat transfer) at the surface is zero. Another improvement brought on by this work is that the model also deals with isothermal walls.

2.2 An introduction to the current model

The present model is an extension of the one developed by Yang et al., 2016 for the incompressible regime. It is an approach based on the Von Karmann-Pohlhausen integral method, in which a shape function is assumed for the mean velocity profile, and its parameters are determined based on momentum conservation and other fundamental constraints. In order to develop physics-based models for flows over surfaces with attached roughness elements, some detailed understanding of the averaged velocity profile within the roughness layer (defined here as the region between the surface and the top of the roughness elements) must be developed. This is similar to the situation where knowledge about the logarithmic law has led to physically based drag laws for smooth boundary layers. To obtain the mean velocity profile as a function of height, the modelling task focuses on the Reynolds stress (which arises due to temporal averaging over turbulence), the dispersive stress (which arises due to spatial averaging of the mean velocity across spatial heterogeneities in the temporal mean velocity distribution), and the form drag (which arises due to the direct momentum extraction by the roughness elements interacting with the flow). The Reynolds stress is typically modelled with a Prandtl mixing-length eddy-viscosity model, the dispersive stress is commonly neglected, and the drag is typically modelled using a quadratic law for a body force associated with the form drag $F = C_d \rho U^2 \delta A_f / \delta V$, where ρ is the fluid density, C_d is the drag coefficient, U is the mean stream-wise reference velocity and δA_f is the projected frontal area

within a volume δV. The mixing length (denoted as l_m) and the drag coefficient C_d must be specified. With these models for stresses and the force, the spatially and temporally averaged stream-wise momentum equation can be integrated in the wall normal direction to obtain the mean velocity profile.This method leads to the characterisation of an exponential mean velocity profile in the roughness sublayer, derived as a solution of the Reynolds-averaged stream-wise momentum equation.

The main reason why this approach is applicable to the $M = 2$ case is that, even if the external flow is supersonic, down in the boundary layer the velocity is subsonic and near the roughness elements the fluid can be considered incompressible.

Concerning the temperature profiles, they are achieved through the similarity of momentum and energy transport in turbulent flows. This fundamental concept is called the Reynolds analogy.

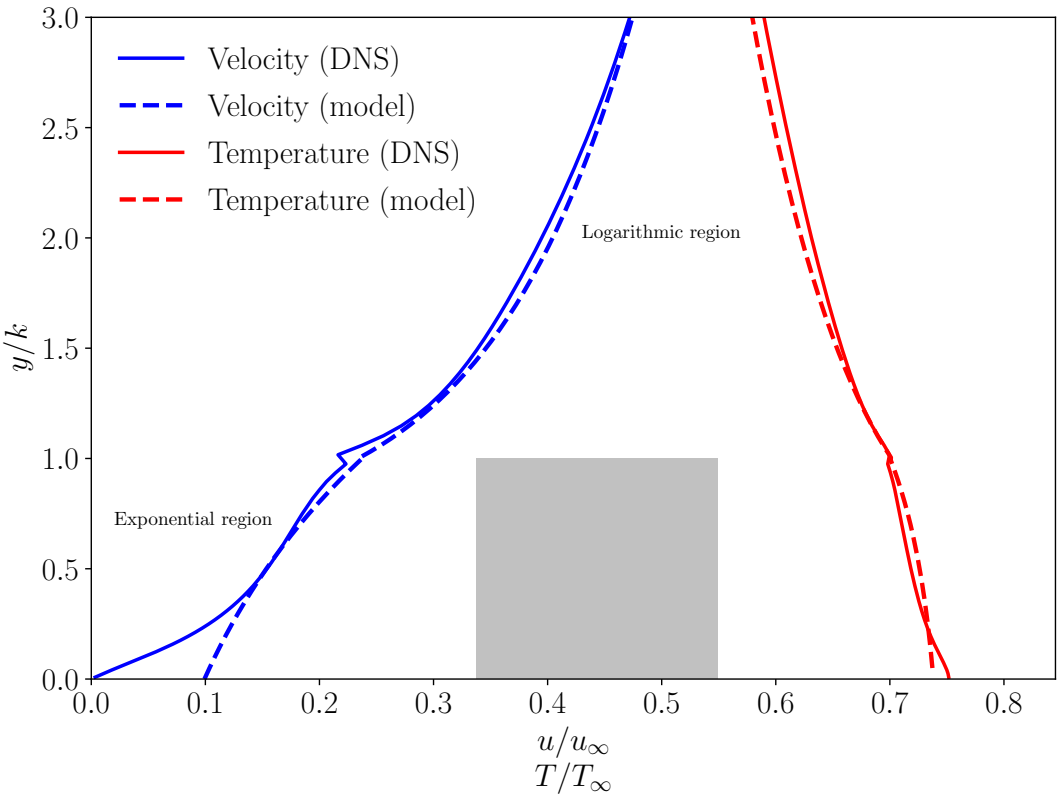

Figure 5: Explanation of the profiles derived in the present model to derive the skin friction and heat transfer at the wall. The modelled velocity and temperature profiles are compared with the DNS data from Cogo et al., 2025.

3. Theoretical background

3.1 Channel flow

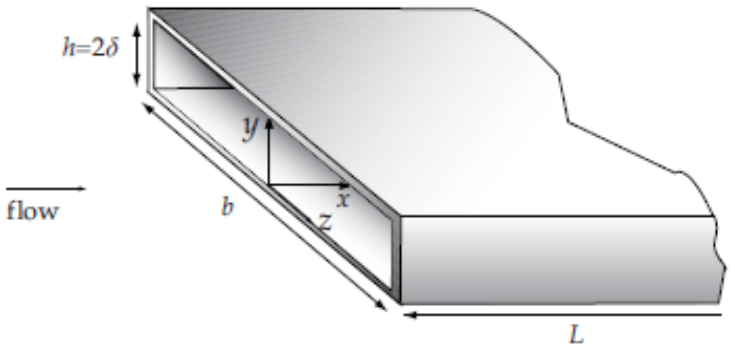

Figure 6: Sketch of channel flow

Most studies of turbulent boundary layers revolve around a simple geometry described by a stationary flow passing through two plates at a certain distance from each other. This setup is convenient because of the symmetry that this problem presents. The distance from the two plates is 2δ and the stream-wise and span-wise dimensions are much larger than the wall-normal one ($L_x >> 2\delta$ and $L_z >> 2\delta$). In this way, the Reynolds averaged velocity statistics do not depend on x and z, so the mean velocity field is described by the vectorial field $\langle\vec{U}\rangle = \langle\vec{U}(y)\rangle$ (Pope, 2000). The Reynolds number is defined as follow:

$$Re = \frac{U_0 \cdot 2\delta}{\nu} \tag{3.1}$$

where:

- U_0 is the bulk velocity;

$$U_0 = \frac{1}{2\delta}\int_0^{2\delta} \langle U(y)\rangle dy \tag{3.2}$$

- δ is the half width of the channel;
- ν is the kinematic viscosity.

The Reynolds number is chosen to be $Re > 3000$ in order to fall in the turbulent regime. From the RANS continuity equation (see Appendix) $\nabla \cdot \langle\vec{U}\rangle = 0$, given the symmetry of this problem and the impermeability boundary condition, we obtain $\langle V\rangle \equiv 0$ for all y. The y component of the momentum equation reduces to:

$$\langle p\rangle + \rho\langle v'^2\rangle = p_w(x); \tag{3.3}$$

where $p_w(x)$ is the mean wall pressure and is only a function of x, so we can write the x component of the momentum equation as follows:

$$\frac{dp_w}{dx} = \frac{d}{dy}\Big[\tau(y)\Big]; \tag{3.4}$$

where $\tau(y)$ is the total mean shear stress:

$$\tau(y) = \mu \frac{d\langle U \rangle}{dy} - \rho \langle u'v' \rangle. \tag{3.5}$$

The first term on the left side of equation 3.5 is the mean viscous stress, while the second term is the turbulent Reynolds stress (which is negligible in the case of laminar flow). Since the left term of equation 3.4 is a function of x and the left term is a function of y, the only possibility for both terms is to be equal to a constant value a. Therefore, from equation 3.4 we obtain:

$$\frac{d}{dy}\left[\tau(y)\right] = a; \tag{3.6}$$

and integrating considering the boundary conditions:

$$\tau(y) = \tau_w \left(1 - \frac{y}{\delta}\right) \tag{3.7}$$

where $\tau_w = \mu \frac{dU}{dy}\Big|_{y=0}$ is the mean wall shear stress (drag per unit area). Also, form equation 3.4 we get:

$$\frac{dp_w}{dx} = a = -\frac{\tau_w}{\delta}; \tag{3.8}$$

which gives:

$$\tau_w = -\frac{dp_w}{dx} \cdot \delta \tag{3.9}$$

Equation 3.9 sets the balance between mean wall shear flow and pressure gradient in x direction.

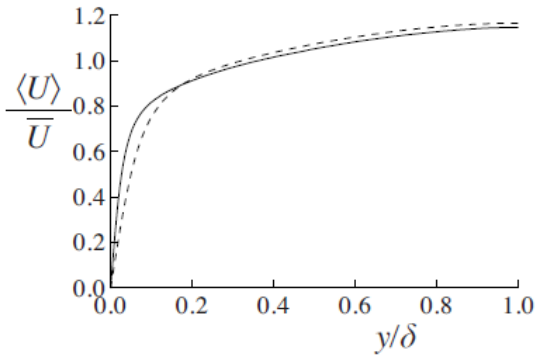

Figure 7: Mean velocity profiles in fully developed turbulent channel flow from the DNS of Kim et al. (1987): dashed line, Re = 5,600; solid line, Re = 13,750. The velocity gradient at the wall increases with the Reynolds number (Pope, 2000).

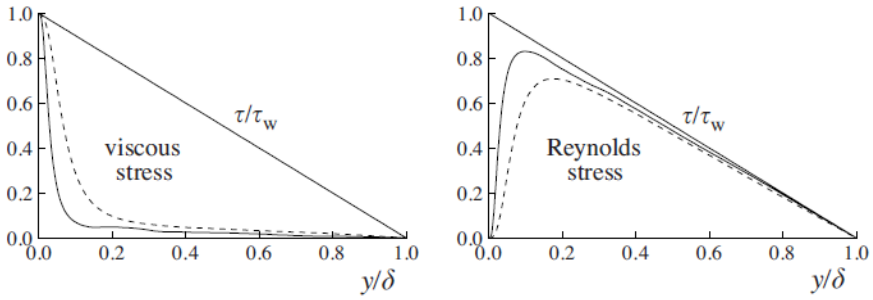

Figure 8: Profiles of the viscous shear stress, and the Reynolds shear stress in turbulent channel flow: DNS data of Kim et al. (1987): dashed line, Re = 5,600; solid line, Re = 13,750. With increasing Re the viscous stress remains dominant in a smaller region near the wall, while the Reynolds stress increases far from the wall (Pope, 2000).

When the Reynolds number increases, it is possible to make some observations:

- the velocity gradient at the wall increases (figure 7), so the total mean shear stress grow up as a consequence $\tau_w = \mu \frac{\partial U}{\partial y}\Big|_{y=0}$;
- the Reynolds stress $-\rho\langle u'v'\rangle$ increases in the region far from the wall;
- the viscous stress $\mu\frac{\partial U}{\partial y}$ become more confined in the near-wall region and there remains dominant (figure 8).

3.1.1 Dimensional theory

We now define some quantities that are used to characterize and distinguish the internal and external regions:

- friction velocity,
$$u_\tau = \sqrt{\frac{\tau_w}{\rho}}; \tag{3.10}$$
- viscous length,
$$\delta_\nu = \frac{\nu}{u_\tau} = \frac{\mu}{\rho u_\tau}; \tag{3.11}$$

In the external region ($y >> \delta_\nu$ or $\frac{y}{\delta_\nu} >> 1$) the characteristic velocity and length-scale are u_τ and δ, while in the internal region ($y << \delta$ or $\frac{y}{\delta} << 1$) we use u_τ and δ_ν. The friction Reynolds number, Re_τ, tells us the separation between the two regions and it is defined as follow:
$$Re_\tau = \frac{\delta}{\delta_\nu} = \frac{h u_\tau}{\nu}; \tag{3.12}$$
for example, $Re_\tau = 1000$ indicates that the internal region, where viscous effects are important, is one thousand times smaller than the channel half-width.

3.1.2 Determination of velocity profiles

The impermeability sets the mean velocity to be zero at the wall ($\langle U(y=0)\rangle = 0$), so near the wall, we can use a Taylor expansion to describe the profile:

$$\langle U(y)\rangle = \langle U(y=0)\rangle + \left.\frac{d\langle U\rangle}{dy}\right|_{y=0} \cdot y + O(y^2); \tag{3.13}$$

since the first term to the left is zero, we can divide all the equation 3.14 by u_τ and normalize the y coordinate with respect to δ_ν defining a scale coordinate, or wall unit y^+ and a scaled velocity u^+:

$$\frac{\langle U(y)\rangle}{u_\tau} = u^+ = \frac{1}{u_\tau}\left.\frac{d\langle U\rangle}{dy}\right|_{y=0} \cdot y^+ \cdot \delta_\nu + O(y^2); \tag{3.14}$$

where $y^+ = \frac{y}{\delta_\nu}$. Neglecting higher-order terms and introducing the definition of viscous length from equation 3.11, we get that the term that multiplicate y^+ in equation 3.14 is:

$$\frac{\delta_\nu}{u_\tau}\left.\frac{d\langle U\rangle}{dy}\right|_{y=0} = \frac{1}{\rho u_\tau^2}\mu\left.\frac{d\langle U\rangle}{dy}\right|_{y=0} = \frac{1}{\tau_w}\cdot\tau_w = 1 \tag{3.15}$$

Therefore, the profile near the wall has to be linear for a few wall units:

$$u^+ = y^+ \tag{3.16}$$

This layer is called viscous sub-layer and holds for $0 \leqslant y^+ \leqslant 5$. Notice that y^+ is similar to a local Reynolds number, so its magnitude can be expected to determine the relative importance of viscous and turbulent processes. In support of this assumption, figure 9 shows the fractional contributions to the total stress from viscous and Reynolds stresses in the near-wall region of channel flow. When they are plotted against y^+, the profiles for the two Reynolds numbers almost collapse. The viscous contribution drops from 100% at the wall ($y^+ = 0$) to 50% at $y^+ \simeq 12$ and is less than 10% by $y^+ = 50$. Different regions, or layers, in the near-wall flow are defined on the basis of y^+. In the viscous wall region $y^+ < 50$, there is a direct effect of molecular viscosity on the shear stress; whereas, conversely, in the outer layer $y^+ > 50$ the direct effect of viscosity is negligible. Within the viscous wall region, in the viscous sublayer $y^+ < 5$, the Reynolds shear stress is negligible compared with the viscous stress, but the departures from the linear relationship are significant (greater than 25%) for $y^+ > 12$. As the Reynolds number of the flow increases, the fraction of the channel occupied by the viscous wall region decreases, since δ_ν/δ varies as Re_τ^{-1}.

The inner layer is usually defined as $y/\delta < 0.1$. At high Reynolds number, the outer part of the inner layer corresponds to large y^+, i.e., $y^+ \simeq 0.1\delta/\delta_\nu = 0.1Re_\tau >> 1$. As has already been discussed, for large y^+ it can be assumed that viscosity has little effect. Fully developed channel flow is completely specified by ρ, ν, δ, and u_τ. There are just two independent non-dimensional groups that can be formed from these variables and the y coordinate (e.g., y/δ and $Re_\tau = u_\tau\delta/\nu$) and consequently the mean velocity profile can be written:

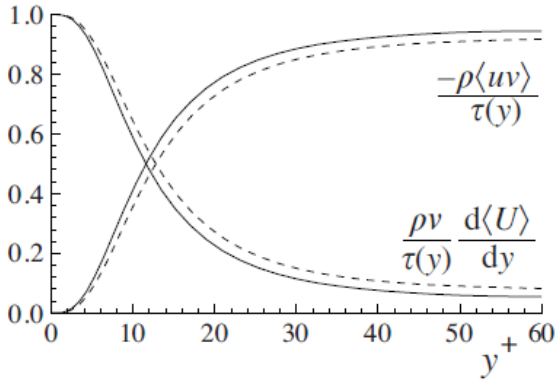

Figure 9: Profiles of the fractional contributions of the viscous and Reynolds stresses to the total stress. DNS data of Kim et al. (1987): dashed lines, Re = 5,600; solid lines, Re = 13,750 (Pope, 2000).

$$\langle U\rangle = u_\tau F_0\left(\frac{y}{\delta}, Re_\tau\right) \tag{3.17}$$

where F_0 is a universal non-dimensional function to be determined. Although this approach to determining the mean velocity profile appears natural, it is, however, preferable to proceed somewhat differently. Instead of $\langle U\rangle$, consider the velocity gradient $d\langle U\rangle/dy$, which is the dynamically important quantity. The viscous stress and the turbulence production, for example, are both determined by $d\langle U\rangle/dy$. Again on dimensional grounds, $d\langle U\rangle/dy$ depends on just two non-dimensional parameters:

$$\frac{d\langle U\rangle}{dy} = \frac{u_\tau}{y}\Phi\left(\frac{y}{\delta_\nu}, \frac{y}{\delta}\right) \tag{3.18}$$

where Φ is a universal non-dimensional function. The idea behind the choice of the two parameters is that δ_ν is the appropriate length-scale in the viscous wall region ($y^+ < 50$) while δ is the appropriate scale in the outer layer ($y^+ > 50$). As has already been discussed, in the inner layer ($y/\delta < 0.1$), for large y^+ it can be supposed that viscosity has little effect. Hence, in equation 3.18, the dependence of Φ on ν (through δ_ν) and δ vanishes, so that Φ adopts a constant value:

$$\Phi = \frac{1}{\kappa}, \quad \text{for} \quad \frac{y}{\delta} << 1 \quad \text{and} \quad y^+ >> 1 \tag{3.19}$$

Thus, in this region, the mean velocity gradient is

$$\frac{du^+}{dy^+} = \frac{1}{\kappa y^+} \tag{3.20}$$

which integrates to

$$u^+ = \frac{1}{\kappa} ln(y^+) + B \tag{3.21}$$

This is the logarithmic law of the wall due to Von Karman (1930) or simply, the log-law and κ is the von Karman constant. In the literature, there is some variation in the values ascribed to the log-law constants, but generally they are within 5% of

$$\kappa = 0.41, \quad B = 5.2 \tag{3.22}$$

Figure 10 shows a comparison between the log law and the DNS data in the inner part of the channel ($y/\delta < 0.25$). Clearly, there is excellent agreement for $y^+ > 30$.

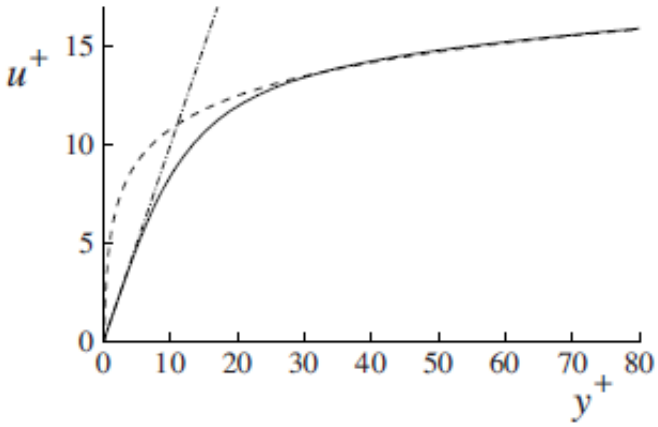

Figure 10: Near-wall profiles of mean velocity: solid line, DNS data of Kim et al. (1987): $Re = 13,750$; dot–dashed line, $u^+ = y^+$; dashed line, the log law (Pope, 2000).

The region between the viscous sublayer ($y^+ < 5$) and the log-law region ($y^+ > 30$) is called the buffer layer. It is the transition region between the viscosity-dominated and the turbulence-dominated parts of the flow. This layer does not have a well-specified law that describes the velocity profile due to the self-sustained cycle of turbulence. The various regions and layers that are used to describe near-wall flows are summarised in figure 11.

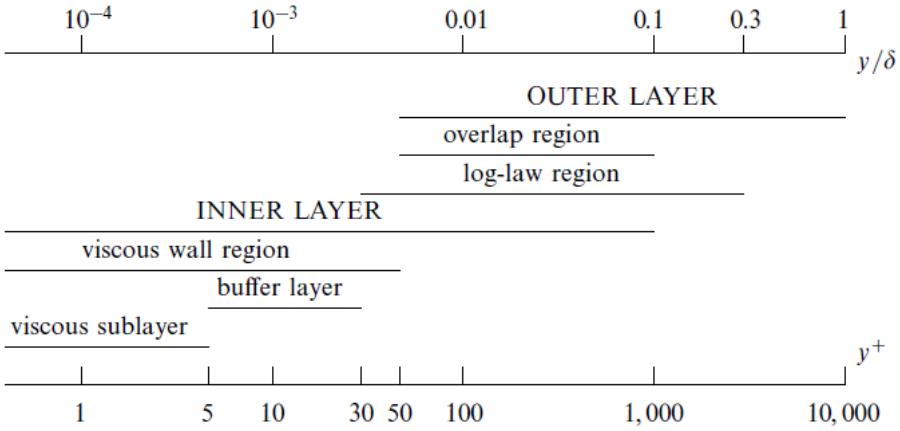

Figure 11: A sketch showing the various wall regions and layers defined in terms of $y^+ = y/\delta_\nu$ and y/δ, for turbulent channel flow at high Reynolds number, $Re_\tau = 10^4$ (Pope, 2000).

3.2 Roughness theory

In this section, the fundamental aspects of the topic are discussed. They revolve mostly around the incompressible regime, since the researchers have found a general consensus, at least for the basic theory. Many members of the scientific community are committed to the development of simple previsional models that are applicable in short time to avoid executing heavy simulations. The major obstacle is represented by the behaviour of the flow near the wall; it is very difficult to understand a priori (without making an experiment or a simulation) how the fluid will perceive the asperities.

Basically, whether a surface is considered smooth or rough, it depends not only on the topography of the surface but also on the behaviour of the flow that occurs next to it. So, a surface that is considered rough from a geometrical point of view, can be considered smooth by the fluid if the asperities are not big enough to influence the dynamics of its motion. There are a few parameters that can be used to evaluate the regime of motion. First, it is important to recognise that turbulence is characterised by two length-scales in the boundary layer, as discussed in the precious section: the boundary layer thickness δ and the viscous length-scale δ_ν.

δ_ν is the relevant scale near the wall, where viscosity is more important. Given the roughness height k, if its ratio with the boundary layer thickness $\frac{\delta}{k}$ is not great enough, the flow will not display a clear separation of the inner and outer scales, leading to a configuration known as "flow through obstacles". The condition to avoid this scenario is (Jiménez, 2004):

$$\frac{\delta}{k} \gtrsim 40 \tag{3.23}$$

The choice of the roughness height depends on context and application (it could be the mean value, the root mean square value or the peak-to-trough value) but, in any case, it needs to display a separation from the viscous length-scale and to evaluate that, a parameter called roughness Reynolds number,k^+, is introduced and it is crucial to determine the regime of motion of the flow.

$$k^+ = \frac{k}{\delta_\nu} \tag{3.24}$$

However, the literature refers mainly to a similar parameter, called the equivalent roughness Reynolds number, k_s^+, which use the equivalent sand grain height k_s instead of k. This choice descends from the studies of Nikuradse (1933) on the matter who used to cover pipes with sand to evaluate pressure losses. k_s defines the grain size of uniform (mono-disperse), close-packed sand grains on a hypothetical surface that would cause the same drag as the surface of interest if exposed to the same flow in the fully rough regime. It does not measure a physical distance, rather, it is a hydraulic scale defined by drag that must be determined from experiments or simulations for a specific surface roughness.

$$k_s^+ = \frac{k_s}{\delta_\nu} \tag{3.25}$$

Therefore, the three different regimes are as follows:

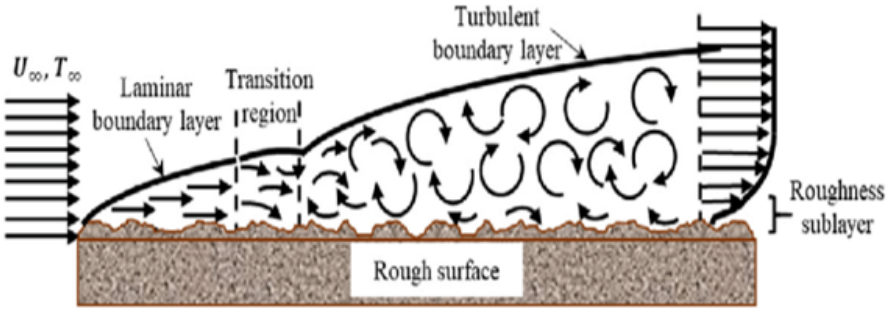

Figure 12: Typical development of a turbulent boundary layer over a rough surface. The roughness sub-layer substitutes the viscous sub-layer present in the smooth cases.

- hydraulically smooth if $k_s^+ \leqslant 5$, there is no additional drag caused by roughness and the flow perceives the surface as smooth;
- transitionally rough if $5 \leqslant k_s^+ \leqslant 70$, the additional drag is due to both viscous and pressure drag;
- fully rough if $k_s^+ \geqslant 70$, the additional skin friction does not depend on viscosity anymore, but only on pressure drag.

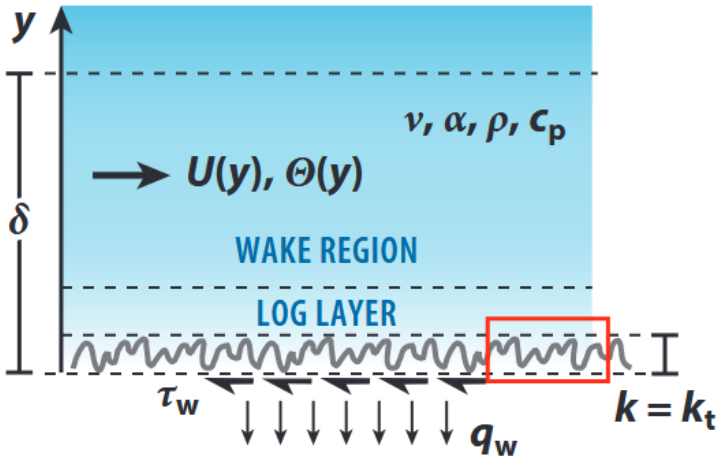

Figure 13: Typical layer stratification of a boundary layer. $k = k_t$ could be a parameter of choice that describe the roughness height (mean value, rms value, maximum peak to through value, etc.). In this figure $U(y)$ and $\Theta(y)$ are the mean velocity and temperature profiles of the flow characterised by a density ρ, kinematic viscosity ν, specific heat c_p, and thermal diffusivity α (Chung et al., 2021).

The boundary layer presents different structures due to the length-scales that control the inner region. In the outer region, the flow statistics show some similarities, independently of the roughness presence. This outer layer similarity was hypothesized by Townsend, 1980 and articulated by Raupach et al., 1991.It states that only u_τ and δ are relevant in the outer layers if sufficiently large scale separation is achieved. An important aspect to consider when assessing outer-layer similarity is the zero-plane displacement, d, also known as the wall offset. The y- coordinate is

often measured from a reference plane, such as the bed on which roughness elements are mounted. However, the outer turbulent flow does not perceive its origin to be at $y = 0$ but at $y = d$. The offset is typically between the crest and trough of roughness elements, and depends not only on the roughness topography but also on the roughness Reynolds number. If the spacing between roughness elements is small relative to viscous scales, $y = d$ approaches the crest because the flow behaves as if a smooth wall were located at the crest(Raupach et al., 1991).

3.3 Roughness sublayer

Each roughness topography has a specific flow signature near the wall. For example, the flow can resemble flow over bluff bodies, including separated flow with reattachment regions and shed vortices. This roughness-affected region near the wall is labelled the roughness sublayer ($y < y_r$), the extent of which is roughness dependent. In this region the flow is clearly influenced by the local roughness topography. Jiménez, 2004 and Raupach et al., 1991 suggested that y_r might be two to five times k but it is not obvious which roughness height k to use in general.

3.4 Logarithmic law

In turbulent wall-bounded flow over smooth walls, when $k^+ << 1$, the roughness is submerged below the viscous sublayer and the surface appears smooth to the flow. If the friction Reynolds number $Re_\tau = \frac{\delta}{\delta_\nu}$ is sufficiently large , an inertial range of y, where viscosity does not directly matter, can emerge near the wall that is independent of the outer-flow geometry. In this layer the scaled velocity has a logarithmic relation with the scaled y-coordinate:

$$u_S^+ = \frac{1}{\kappa} ln(y^+) + A \tag{3.26}$$

where $\kappa \simeq 0.4$ is the Von Karman constant and $A \simeq 5.2$ is an integration constant obtained experimentally. The subscript "S" stands for smooth-wall conditions. When the wall is rough such that k^+ is no longer small, there is the additional requirement of y that need to be far above the direct influence of roughness ($y/k >> 1$), i.e., above the roughness sublayer. Then, the log-law assumes a new form:

$$u_R^+ = \frac{1}{\kappa} ln\left(\frac{y}{k}\right) + B\left(\frac{y}{k}\right) \tag{3.27}$$

where B is a function of both the roughness topography and the roughness Reynolds number k^+ and the subscript "R" indicates rough-wall conditions. If viscous effects can be neglected and $k^+ >> 1$, the intercept B approaches a finite value $B(\infty)$ that depends only on the roughness topography, independently of the roughness Reynolds number k^+. The appearance of a log-law has often been taken as evidence of outer-layer similarity. The effect of a given rough surface boils down to determining the unknown function, $B(k^+)$. For precision, y should be replaced by $y - d$ near the roughness in equation 3.27 to account for the offset of the turbulent flow.

3.5 Roughness function

A convenient and intuitive way to describe the log-law intercept $B(k^+)$ is through the roughness function $\Delta u^+(k^+)$, defined by Hama (1954) and given by the shift at matched y+ of the rough-wall log law relative to that of the smooth wall. Subtracting 3.26 and 3.27 gives:

$$\Delta u^+(k^+) = u_S^+ - u_R^+ = \frac{1}{\kappa} ln(k^+) + A - B(k^+) \tag{3.28}$$

It indicates the momentum deficit resulting from surface roughness and thus can be interpreted as a measure of the drag penalty relative to a smooth wall: drag increases for $\Delta u^+ > 0$ and drag reduces for $\Delta u^+ < 0$. For $\Delta u^+ = 0$, the surface remains hydrodynamically smooth because viscosity damps out the roughness-induced turbulent fluctuations that would otherwise slow down the flow. As k^+ increases, the onset of roughness effects occur, $\Delta u^+ \gtrsim 0$, and the flow is said to be transitionally rough. In this roughness regime, both viscous and pressure drag on the roughness elements contribute to skin friction. As k^+ increases further, pressure drag dominates. In this so-called fully rough regime, the skin-friction coefficient becomes independent of Reynolds number ($Re_\delta = \delta U_\delta / \nu$). Every rough surface has a possibly distinct $\Delta u^+(k^+)$, not only in the value of the fully rough intercept $B(\infty)$ but also in the behaviour of the transitionally rough regime. This is what makes the prediction of drag due to rough surfaces so difficult.

When using the equivalent roughness Reynolds number k_s^+ the roughness function become:

$$\Delta u^+(k_s^+) = \frac{1}{\kappa} ln(k_s^+) + A - B_s(k_s^+) \tag{3.29}$$

where $B_s(k_s^+)$ is the intercept measured by Nikuradse (1933) for uniform sand grains and its value in the limit of the fully rough regime is $B(\infty) = 8.5$. By equating 3.28 and 3.29 in the fully rough regime, it is possible to extrapolate a relationship that converts the physical roughness size k into the hydraulic scale k_s:

$$\frac{k_s}{k} = e^{[\kappa(B_s(\infty) - B(\infty)]} \tag{3.30}$$

Without the fully rough condition, B_s and B remain functions of k_s^+ and k^+, respectively, and matching equations 3.28 and 3.28 yields a ratio k_s/k that is a function of k^+.

Another parameter is used in meteorology to describe the u_R^+ profile instead of k_s, and it is the roughness length, y_0:

$$u_R^+ = \frac{1}{\kappa} ln\left(\frac{y}{y_0}\right) \tag{3.31}$$

Basically, it is the location $y = y_0$ where the log-law extrapolates to $u_R^+ = 0$. Subtracting 3.26 with 3.31 gives:

$$\Delta u^+ = \frac{1}{\kappa} ln(y_0^+) + A \tag{3.32}$$

Confronting this expression with 3.29 in the fully rough regime gives:

$$\frac{y_0}{k_s} = e^{-\kappa B_s(\infty)} \simeq 1/30 \tag{3.33}$$

3.6 Surface properties

What topographical properties exert an influence on the flow and what is the bare minimum set of these properties that would be required to estimate the drag of a surface? Surface roughness is most of the time caused by random processes which are difficult to predict or not predictable at all in many cases thus leading to countless surface morphologies that cannot be easily defined. Thus, a great deal of research has been directed at attempts to correlate topographical features to k_s (Chung et al., 2021).

$$k_s = f(topographical\ properties) \tag{3.34}$$

The first step is to adopt clearly defined and measurable surface parameters.

3.6.1 Roughness height

It can be defined in various ways:

- average roughness height, k_a

$$k_a = \frac{1}{A_t}\int |h'| dA \tag{3.35}$$

  where h' is the variation in roughness elevation about the mean and A_t is the total plan area;

- root-mean-square roughness height, k_{rms}

$$k_{rms} = \sqrt{\frac{1}{A_t}\int h'^2 dA} \tag{3.36}$$

  that is the standard deviation of roughness elevation;

- maximum peak-to-trough roughness height, k_t

The former two, which involve area integrals, are less subject to corruption by extreme asperities and thus represent more reliable statistical measures of mean roughness amplitude.

3.6.2 Frontal solidity

Frontal solidity $\lambda_f$is simply the ratio of the projected frontal area, A_f, of roughness elements to the total plan area, A_t.

$$\lambda_f = \frac{A_f}{A_t} \tag{3.37}$$

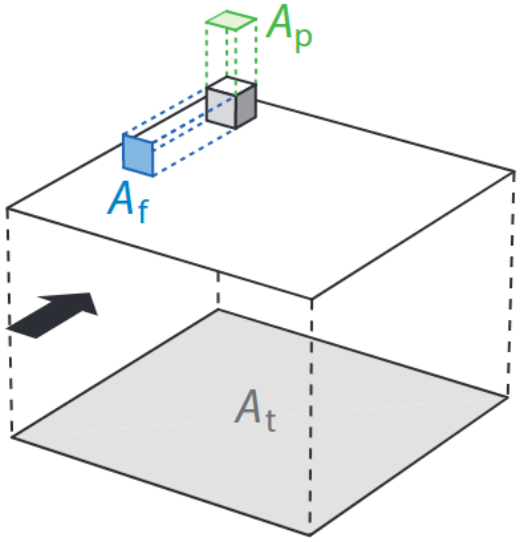

Figure 14: Surface sketches to illustrate frontal area, A_f and plan area, A_p (Chung et al., 2021)

Frontal solidity measures the available area exposed to pressure drag. Very sparsely packed or isolated roughness elements ($\lambda_f \to 0$, fig 15a) will tend toward smooth conditions since there will be increasing expanses of smooth-like conditions between elements, as will very densely packed roughness where individual elements will be sheltered due to proximity to neighbours (fig 15b).

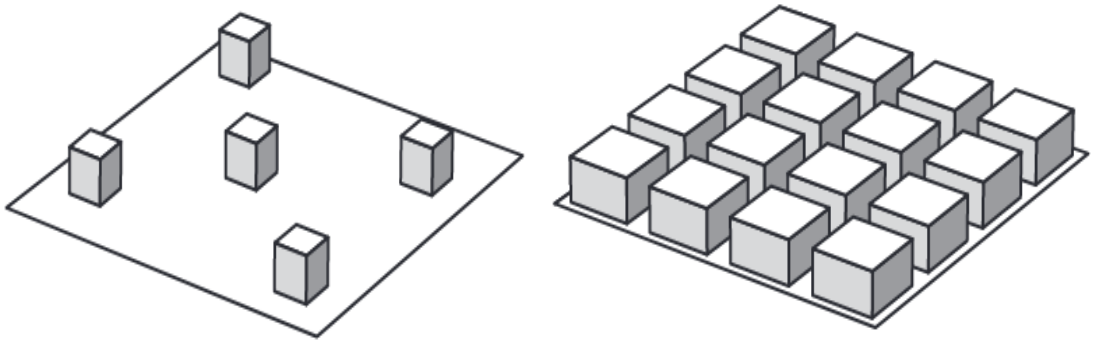

(a) (b)

Figure 15: Examples of sparse (a) and dense (b) frontal solidity λ_f Chung et al., 2021.

Typically, the maximum in drag occurs between these regimes, at $0.1 \lesssim \lambda_f \lesssim 0.3$.

3.6.3 Plan solidity

When combined with λ_f, plan solidity λ_p, defined as the ratio of the plan area, A_p, of roughness elements to the total plan area, A_t can give an improved measure of the roughness form (fig 14):

$$\lambda_p = \frac{A_p}{A_t} \tag{3.38}$$

The ratio of λ_f/λ_p can, in some scenarios, give an indication of the aspect ratio of the roughness elements. For example, a cube-like element will have $\lambda_f/\lambda_p = 1$, a squat element will have $\lambda_f/\lambda_p < 1$, and tall thin elements will have $\lambda_f/\lambda_p > 1$. Such generalisations can be corrupted in situations where elements are clustered.

3.6.4 Skewness

A measure of the asymmetry in surface-elevation distribution is skewness, Sk. In general, pitted surfaces will be negatively skewed and surface deposits will be positively skewed. For wall-mounted cubes (fig 14), a measure of skewness is conveyed by the plan solidity λ_p, where $\lambda_p > 0.5$ implies $Sk < 0$ and vice versa:

$$Sk = \frac{1 - 2\lambda_p}{[\lambda_p(1 - \lambda_p)]^{1/2}} \tag{3.39}$$

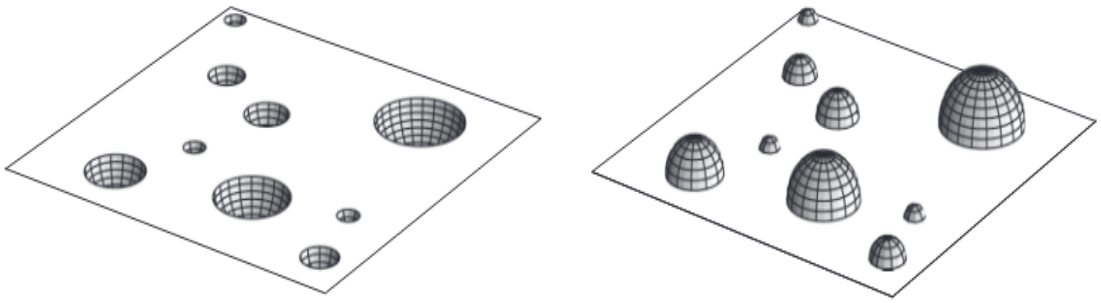

(a) (b)

Figure 16: Examples of negatively skewed (a) and positively skewed (b) surfaces (Chung et al., 2021).

Skewness is also very important for compressible flows; when the high-speed flux encounters a pitted surface, it generates an expansion fan, when there is an obstacle like a deposit, it generates a shock wave.

3.6.5 Clustering

Roughness height, skewness, and frontal and plan solidity fail to capture clustering or spatial homogeneity. The examples shown in fig 17, all have the same k_a, Sk, λ_f, and λ_p (due to their identical elevation distributions), yet the 16 elements per unit plan area are arranged in very different manners, with different expected outcomes on the flow.

3.6.6 Directionality

The concept of directionality, or anisotropy, is due to either shape or alignment of roughness elements. The anisotropic roughness shown in fig 18 has aligned features, where we may expect the pressure drag (and λ_f) to be very different if the flow were from the direction of the open or closed arrow.

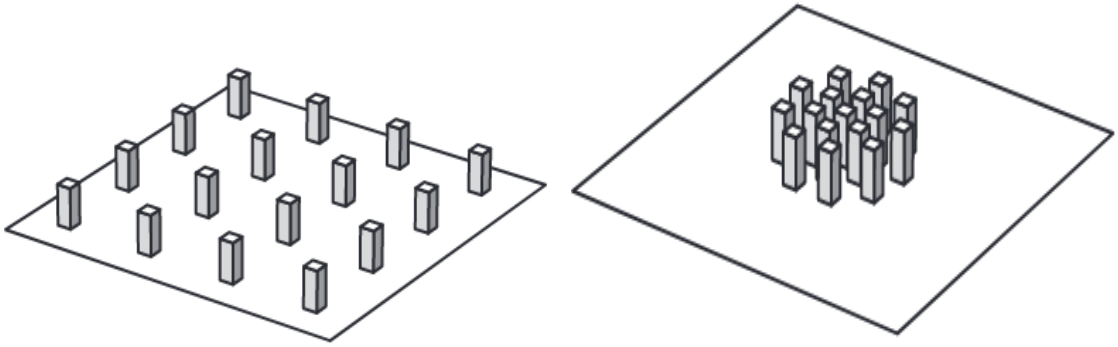

(a) (b)

Figure 17: Surface sketches of clustering (Chung et al., 2021).

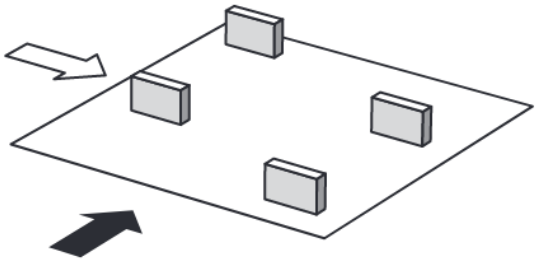

Figure 18: Directionality is important in determining how to calculate the frontal solidity correctly (Chung et al., 2021).

3.7 Compressible roughness

In his survey, Bowersox, 2007 stated that the literature on roughness effects at high speed is limited in terms of data and theoretical approaches to understand the problem. It is known that boundary layers are responsible for skin friction drag and convection heat transfer and that roughness increases these engineering quantities and enhances the transition from laminar to turbulent flow. Unfortunately, most of the data available at that time did not even meet the requirements defined by Jiménez, 2004 in terms of k_s^+ and δ/k. However, for those cases that fell in the fully rough regime, the scaling for high-speed turbulent boundary layers appears to be well correlated with van Driest theory, but results were mostly limited to adiabatic flows.

Supersonic flow over rough surfaces can generate shock and expansion waves that can interact with turbulence all the way across the boundary layer, as observed by Latin et al., 2000. This is especially true at high Mach numbers and Reynolds numbers, where most of the boundary layer is supersonic. Hence, the presence of relatively small roughness elements could generate significant compressibility effects across the boundary layer.

However, what has been discussed for the velocity shift in the incompressible regime, can be used with a similar approach for the temperature, where

$$T_\tau = \frac{q_w}{\rho c_p u_\tau} \tag{3.40}$$

is the friction temperature (q_w is the wall heat flux or heat transfer per unit area and c_p is the specific heat at constant pressure) and

$$T^+ = \frac{T}{T_\tau} \tag{3.41}$$

is the scaled temperature.

4. Near wall modelling of rough wall

4.1 Derivation of the model for momentum

Yang et al., 2016 showed clear evidence of the exponential behaviour of the mean flow within the roughness layer with respect to the wall-normal distance. The approach is based on the von Karman–Pohlhausen integral method, in which a shape function is assumed for the mean velocity profile $U(y)$ and its parameters are determined based on momentum conservation and other fundamental constraints. Writing the Reynolds-averaged stream-wise momentum equation, in which the vertical gradient of the momentum flux (modelled with a constant mixing-length eddy viscosity) balances the distributed drag from roughness elements,

$$\frac{\mathrm{d}}{\mathrm{d}y}\left[l_m^2\left|\frac{\mathrm{d}U(y)}{\mathrm{d}y}\right|\frac{\mathrm{d}U(y)}{\mathrm{d}y}\right] = C_d U(y)^2 \frac{\mathrm{d}A_f}{\mathrm{d}V} \tag{4.1}$$

where dA_f/dV is the projected frontal area per unit volume, and l_m and C_d are the mixing length and drag coefficient respectively, it can be seen that an exponential function of y, $U(y) \sim exp(y)$ solves 4.1:

$$U(y) = U_h e^{[a(y-h)/h]} \tag{4.2}$$

where h represents the height of the roughness elements, U_h is the velocity at $y = h$ and a is the attenuation factor, which depends on the parameters in 4.1 and will be explained later using the sheltering mechanism. l_m and C_d can be dependent on y, but are assumed to be constant in order to derive a simple solution, while U_h and a depend on the local surface morphometric properties and flow configurations in the roughness sublayer. For what concern the mean profile at $y > h$, the present model assumes a standard logarithmic law:

$$U(y) = \frac{u_\tau}{k}\big[ln[(y-d)/z_0] + \Pi W(y/\delta)\big] \tag{4.3}$$

where k is the von Karmann constant, δ is the boundary layer thickness and $\Pi W(z/\delta)$ is a wake function with the parameter Π typically of order unity. u_τ is the friction velocity, z_0 is the hydrodynamic roughness length (the height of roughness elements perceived by the flow) and d is the displacement height (the shift of the origin of the profile from the wall perceived by the flow).

Since in the log-layer, compressibility effects must be accounted for, the profile is derived with respect to y and complemented by the Van Driest compressible transformation (Van Driest, 1951):

$$\frac{du}{dy} = \frac{u_\tau}{k}\frac{1}{y-d}\sqrt{\frac{\rho_w}{\rho}} + \frac{u_\tau}{\delta}\frac{\Pi}{k}\pi \ \sin\left(\pi\frac{y}{\delta}\right) \tag{4.4}$$

At $y = \delta$, the profile becomes constant $U(y) = U_0$, the free-stream velocity. The expected profile is shown in figure 19.

It should be noted that the profile does not vanish at $y = 0$, but for now we are not interested in an additional, possibly very thin, additional layer in which the velocity rapidly decreases to zero.

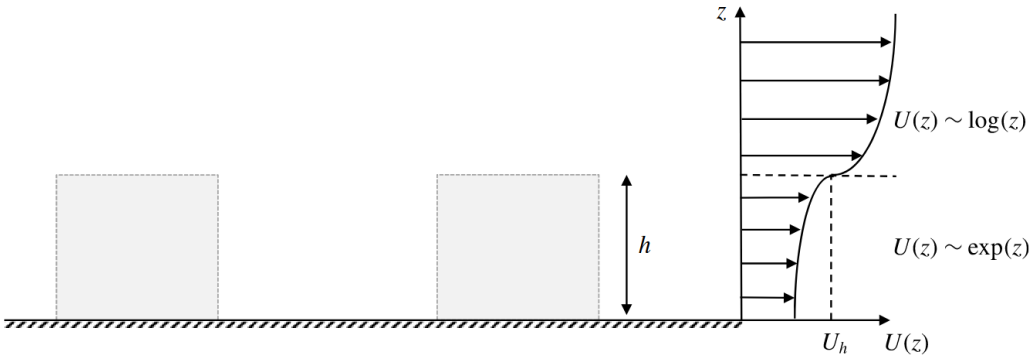

Figure 19: Assumed mean velocity profile $U(z)$.From top to bottom a standard logarithmic layer characterized by roughness and displacement lengths, and friction velocity (and further above possibly a wake), and an exponential layer characterized by the roughness element height and an attenuation coefficient (Yang et al., 2016).

To fully characterise the profiles described in 4.2 and 4.4, five parameters are required: U_h, u_τ, d, z_0, a, while information about U_0, δ, h and the geometrical distribution of the roughness elements are known. These 5 unknowns need 5 constraints: one can be found based on the basic principle of momentum balance and two from continuity of the velocity profile. A fourth fundamental constraint is based on the relation of the displacement height d to the centre of force, the height at which the effective wall stress is to be applied by the roughness elements to the flow. The fifth constraint determines the exponential attenuation coefficient a and is discussed later, based on considerations of flow sheltering.

The first is obtained by the vertical integration of the momentum balance between the downward momentum flux within the inertial layer and the form drag due to roughness:

$$A_T u_\tau^2 = \int_{A_f} C_d U(y)^2 dA_f \tag{4.5}$$

For the right-hand side the quadratic law for the form drag is employed, while the viscous skin friction is not considered, based on the assumption of a fully-rough regime. Substituting 4.2 in 4.5 and integrating from $y = 0$ to $y = h$, assuming $C_d = 1$, the relation for rectangular prism roughness elements become:

$$u_\tau^2 = \frac{1 - e^{-2a}}{2a} \lambda_f C_d U_h^2 \tag{4.6}$$

where $\lambda_f = A_f/A_T$ is the frontal solidity, where A_f and A_T are the projected frontal and horizontal lot areas, respectively.

The second condition is related to the continuity of the velocity profile imposed at $y = h$, so by equating 4.2 and 4.3:

$$\frac{U_h}{u_\tau} = \frac{1}{k} ln\left(\frac{h - d}{z_0}\right) \tag{4.7}$$

where the wake component is negligible $W(h/\delta) \sim 0$ (an assumption that requires the outer layer similarity to hold, $h/\delta << 1$). The continuity is imposed using 4.3 and not the differential law 4.4, because at $M_\infty = 2$, the density variation from ρ_w is considered negligible at $y = h$.

The third constraint is the continuity at $y = \delta$. This equation is posed in an integral form, since the velocity profile is modified by density variations along the log-layer. By equating the integral of 4.4 and U_0:

$$\int_{y=h}^{y=\delta} \frac{du}{dy}\, dy = U_0 - U_h = \int_{y=h}^{y=\delta} \frac{u_\tau}{k}\frac{1}{y-d}\sqrt{\frac{\rho_w}{\rho}} + \frac{u_\tau}{\delta}\frac{\Pi}{k}\pi\ \sin\left(\pi\frac{y}{\delta}\right) dy \tag{4.8}$$

Fourth, the displacement height d can be set equal to the centroid height of the distributed drag force, namely:

$$d = \frac{\int_{A_f} C_d U(y)^2 y dA_f}{\int_{A_f} C_d U(y)^2 dA_f} \tag{4.9}$$

Again, for single-height rectangular-prism roughness, substituting the exponential profile from 4.2 and integrating from $y = 0$ and $y = h$, 4.9 simply leads to:

$$\frac{d}{h} = \frac{1}{1-e^{-2a}} - \frac{1}{2a} \tag{4.10}$$

Combining equations 4.5, 4.7 and 4.10, an expression for z_0 is soon obtained:

$$\frac{z_0}{h} = \left(1 - \frac{d}{h}\right) exp\left[\frac{-k}{\sqrt{\frac{1}{2a}C_d\lambda_f(1-e^{-2a})}}\right] \tag{4.11}$$

The fifth condition to determine the attenuation coefficient a is based on the concept of mutual sheltering.

4.1.1 Sheltering mechanism

This section explains the reduction in the momentum in the wakes of rectangular-prism roughness elements and its effects upon the drag on neighbouring roughness elements. Jiménez, 2004 distinguished two extremes denoted as "d-type" and "k-type" roughness. In the first case each element behave like a shield for the others and the flow can "skim-over" them, while in the second case each elements produces considerable drag since they are more distributed.

Now consider figure 21(a). In the wake of rectangular-prism roughness elements there is a sheltered region in which the velocity is lower than in the unsheltered region. Depending on the spacing between the roughness elements, one may be in a sheltered, unsheltered or 'just sheltered' (i.e. when h_s changes from $h_s = 0$ to $h_s > 0$).

In the "just sheltered" case, the integrated distributed drag equals the drag in the fully exposed frontal area of an individual roughness element (here $A_f = wh$, where w is the width of the element). The latter is assumed to be $C_{DH}U_h^2\ wh/2$,

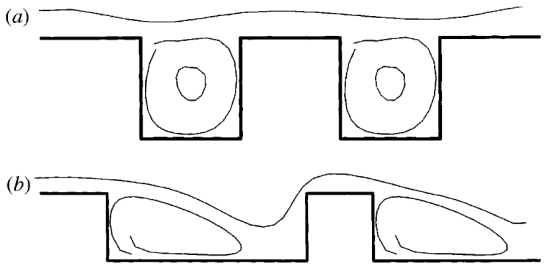

Figure 20: Example of (a) d-type and (b) k-type roughness (Jiménez, 2004).

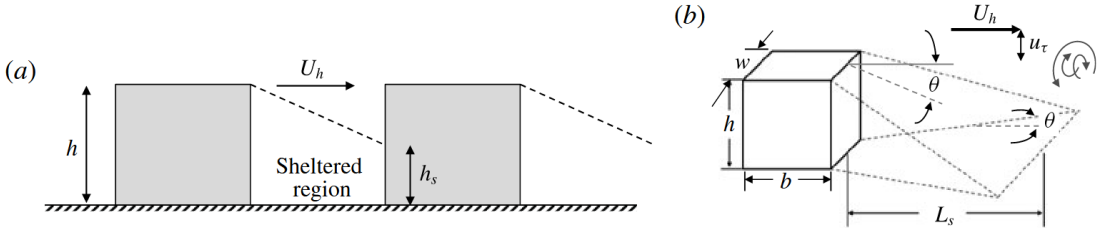

Figure 21: sheltering mechanism for aligned cubical roughness elements. (b) wake geometry: the rate of the wake being 'eaten up' from the top equals the rate at which the wake expands sideways. L_x is the distance between roughness elements and NOT the wake extension (Yang et al., 2016).

where C_{DH} is the drag coefficient (assumed to be known) that expresses the total drag on the element when using the tip velocity U_h as the velocity scale:

$$\int_{A_f} C_d U(y)^2 dA_f = C_d U_h^2 \; wh \frac{1}{2a}[1 - e^{-2a}] = \frac{1}{2} C_{DH} U_h^2 wh \tag{4.12}$$

where $C_{DH} = 1.4$ is the drag coefficient for a surface-mounted cube, and C_d is assumed to be constant. This imply the hypothesis that the drag coefficient for an unsheltered or "just-sheltered" cube is equal to that of an isolated element. So, the condition for a for the 'just sheltered' condition is given by:

$$\frac{1}{2a}[1 - e^{-2a}] = \frac{C_{DH}}{2C_d} \simeq 0.7 \tag{4.13}$$

whose solution is $a \simeq 0.4$. As the roughness elements are placed further distances apart (i.e., by lowering the frontal solidity λ_f), the momentum balance (for fully rough conditions) implies that a remains unchanged at 0.4. Thus, we refer to this value as $a_{min} = 0.4$. As elements are placed closer together, leading to a sheltering effect, we expect a to increase above 0.4, since the velocity profile will be increasingly attenuated to values smaller than U_h as y decreases from $y = h$ downward towards the wall.

In order to determine the value of a that depends on the degree of sheltering, the momentum balance comes again into play. However, because C_{DH} is measured for unsheltered cubes, the momentum balance is only applied for the top portion above the protected region for $y > h_s$ as if the element only protrudes a height h_s

above the surface, thus neglecting the contribution of the sheltered region to drag. The sheltering height h_s depends on the expansion rate of the wake, as shown in figure 21(b), and will be modelled later. For the momentum balance with sheltering the condition become:

$$\int_{h_s}^{h} C_d U(y)^2 w \, dz = \frac{1}{2} C_{DH} U_h^2 w (h - h_s) \tag{4.14}$$

Integrating:

$$\frac{1}{2a(1 - h_s/h)}(1 - e^{-2a(1-h_s/h)}) = \frac{1}{2a_{min}}[1 - e^{-2a_{min}}] \tag{4.15}$$

whose solution is:

$$a = \frac{a_{min}}{1 - h_s/h} \tag{4.16}$$

From 4.16 it is clear that a grows when the elements are closer, in fact the velocity is expected to be lower in the sheltered region.

Figure 21(b) sketches the volume within the wake of a rectangular prism element that has a reduced momentum fluid. Wake expansion in the vertical direction causes a vertical reduction and a span-wise growth of the region of low-momentum fluid. The horizontal convective velocity in the roughness sublayer is of the order of U_h, while the turbulent transport velocity scale in the vertical and span-wise directions is of the order of friction velocity u_τ. As a result, the estimate of the wake expansion rate is as follows:

$$\tan(\theta) = C_\theta \frac{u_\tau}{U_h} \tag{4.17}$$

where C_θ is a coefficient of order unity that may depend on the geometry of the elements. Any portion of a down-stream roughness element that falls in this region of reduced momentum is considered sheltered. The determination of h_s proceeds by calculating the expansion rate using 4.17, and using it to evaluate the area of the sheltered region A_s as the frontal area of the closest rectangular prism roughness elements down-stream. For cases in which sideways growth of the wake causes partial sheltering of the width, the momentum argument presented above is equivalent to setting $h_s = A_s/w$ in 4.14 and thus in 4.16. Depending on the placement of the elements on the surface, the calculation of the sheltered area can be more or less involved. The most general procedure is to, first, find all upstream roughness elements that could shelter the element under consideration and, second, calculate the sheltered frontal area due to each roughness element found in the first step.

For aligned cubic arrays, h_s is simply given as:

$$h_s = max[h - c_\theta(u_\tau/U_h)L_x; 0] \tag{4.18}$$

where L_x is the horizontal distance between the roughness elements.

The wake expansion rate is expressed as 4.17. To estimate the coefficient C_θ, the momentum balance must be evaluated for the case of 'just sheltered' but for various aspect ratios w/h, as sketched in figure 22. The total drag on the element,

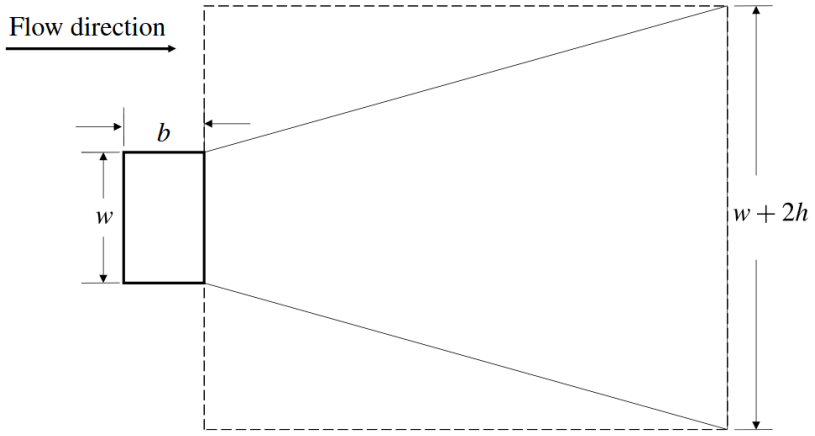

Figure 22: Wake projection: by the time the entire wake is 'eaten away' from the top (i.e. by a distance h), the side expansion is then also h, on both sides. The rectangular region enclosed by the dashed line is argued to carry the vertical flux of momentum associated with the wake growth and vertical reduction of the sheltered region (Yang et al., 2016).

$C_{DH}U_h^2hw/2$, is equated to the vertical momentum flux in the rectangular area of length $h/tan(\theta)$ and width $w+2h$ that is physically associated with wake expansion before the sheltering region has been vertically reduced so that the wake 'touches' the ground (dashed line in figure 22). The width $w+2h$ comes from the fact that the rate at which the wake is 'eaten up' from the top is equal to the rate at which the wake expands sideways, and by the time the entire wake is 'eaten away' from the top (i.e., by a distance h), the side expansion is then also h, on both sides. The vertical flux of momentum per unit area is u_τ^2, thus the balance can be written as:

$$\frac{h}{\tan\theta}(2h+w)u_\tau^2 = \frac{1}{2}C_{DH}hwU_h^2 \tag{4.19}$$

Replacing 4.17 into 4.19 and solving for C_θ leads to:

$$C_\theta = \left(\frac{6}{C_{DH}}\frac{u_\tau}{U_h}\right)\left(\frac{1}{3}+\frac{2h}{3w}\right) \approx O(1)\times\left(\frac{1}{3}+\frac{2h}{3w}\right) = 1-\frac{2}{3}\left(1-\frac{h}{w}\right) \tag{4.20}$$

The validity of 4.20 is associated with the validity of the assumed sheltering region shape in figure 21b. Because such a shape is not physically reasonable for slender 'stick-like' roughness elements, the use of 4.20 should be limited to roughness elements of an aspect ratio h/w that does not exceed an upper threshold. Since the present work involves cubical-shaped elements ($h/w = 1$), the assumptions are valid.

4.2 Sheltering mechanism for staggered cube arrays

This section provides an additional example of calculating the sheltered area analytically for another simple roughness arrangement: the staggered cube arrays. Because all roughness elements will be equally sheltered, the analysis revolves around a single element. Figure 23 sketches the interactions that need to be considered for the particular element A under consideration. The sheltered area of A is determined by:

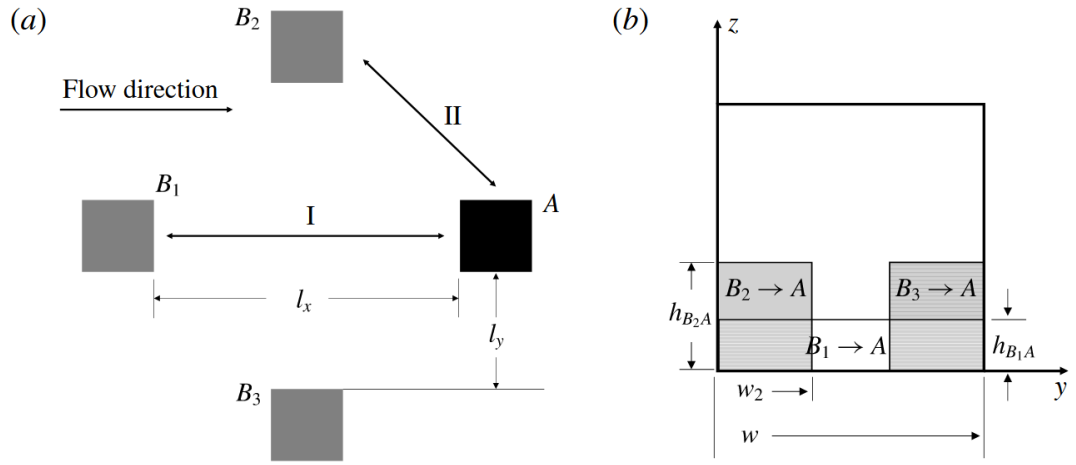

Figure 23: (a) A sketch of the roughness interaction in fully staggered cube arrays. Cube A can be sheltered by B_1, B_2 and B_3. (b) A sketch of the frontal area of A (Yang et al., 2016)

$$A_{s,A} = (w - 2w_2)h_{B_1A} + 2w_2 h_{B_2A} \tag{4.21}$$

where

$$h_{B_1A} = max[0, h - l_x \tan(\theta)], \tag{4.22}$$

$$h_{B_2A} = max[0, h - tan(\theta)(l_x - h)/2] \tag{4.23}$$

and

$$w_2 = max[0, \tan(\theta)(l_x - h)/2 - l_y] \tag{4.24}$$

with

$$l_x = \frac{2h}{\sqrt{\lambda_f}} - h, \quad \text{and} \quad l_y = \frac{h}{\sqrt{\lambda_f}} - h \tag{4.25}$$

4.3 A new proposal for modelling near wall temperature

4.3.1 Temperature and density relations

The first temperature-velocity relationship was presented by Reynolds, 1961 for incompressible flows through the similarity between the Reynolds-averaged momentum and energy equations, the so called Reynolds analogy. This theory was then extended to compressible flows by Busemann (1931) and Crocco (1932), who independently obtained a relation for compressible laminar boundary layers by assuming a unity Prandtl number. Their derivations were extended to turbulent boundary layers by Van Driest, 1951. These studies show that the mean temperature is a quadratic function of the mean velocity:

$$\frac{\bar{T}}{\bar{T}_\delta} = \frac{\bar{T}_w}{\bar{T}_\delta} + \frac{\bar{T}_{c\delta} - \bar{T}_w}{\bar{T}_\delta}\frac{\bar{u}}{\bar{u}_\delta} + \frac{\bar{T}_\delta - \bar{T}_{c\delta}}{\bar{T}_\delta}\left(\frac{\bar{u}}{\bar{u}_\delta}\right)^2 \tag{4.26}$$

where

$$\bar{T}_{c\delta} = \bar{T}_\delta + c\frac{\bar{u}_\delta^2}{2} \tag{4.27}$$

Subscript w denotes the wall and δ denotes the boundary layer edge. c is a parameter that equals one in the Crocco–Busemann relation, but modified to the recovery factor $r \simeq 0.9$ by Walz, 1966 to account for the deviation of Pr from unity. Walz's equation improves the Crocco–Busemann relation and agrees with DNS very well in adiabatic, compressible turbulent boundary layers. However, in diabatic cases, Walz's equation clearly deviates from DNS.

The Generalised Reynolds Analogy proposed by Zhang et al., 2014 has been adopted in the current work to relate the velocity and temperature profiles. It is based on the fact that the RANS equation of stream-wise momentum and energy would display a similarity if $Pr = 1$:

$$\bar{\rho}\bar{u}\partial_x\bar{u} + \bar{\rho}\bar{v}\partial_y\bar{u} = \partial_y\left(\bar{\mu}\partial_y\bar{u} - \overline{\rho u'v'}\right) \tag{4.28}$$

$$\bar{\rho}\bar{u}\partial_x\bar{H} + \bar{\rho}\bar{v}\partial_y\bar{H} = \partial_y\left(\bar{\mu}\partial_y\bar{H} - \overline{\rho H'v'}\right) \tag{4.29}$$

In the case of zero pressure gradient and unity Prandtl number, the solution to these two equations is:

$$\bar{H} - \bar{H}_w = U_w\bar{u} \tag{4.30}$$

To account for the effects of $Pr \neq 1$, wall temperature, pressure gradient, etc., a generalised recovery factor, r_g, is introduced and the solution assumes the form of

$$\bar{H}_g - \bar{H}_w = U_w\bar{u} \tag{4.31}$$

where

$$H_g = c_pT + r_g\frac{u^2}{2} = c_pT_{rg} \tag{4.32}$$

is the general recovery enthalpy and

$$H_w = c_pT_w \tag{4.33}$$

while

$$U_w = -Pr\frac{\bar{q}_w}{\bar{\tau}_w} \tag{4.34}$$

is a proportionality constant with dimension of velocity.
Substituting 4.34 in equation 4.31 leads to:

$$c_p(\bar{T}_{rg} - \bar{T}_w) = -Pr\frac{q_w}{\tau_w}\bar{u} \tag{4.35}$$

where $\tau_w = \rho_w u_\tau^2$, so 4.35 becomes:

$$\frac{c_p \rho_w u_\tau (\bar{T}_{rg} - \bar{T}_w)}{q_w} = -Pr \frac{\bar{u}}{u_\tau} \tag{4.36}$$

that, knowing $T_\tau = q_w/(c_p \rho_w u_\tau)$, finally brings to:

$$\frac{\bar{T}_{rg} - \bar{T}_w}{T_\tau} = -Pr \frac{\bar{u}}{u_\tau} \tag{4.37}$$

From equation 4.37 it is possible to derive the mean temperature profile as a function of the mean velocity, while the generalised recovery factor is calculated as follow:

$$r_g = \frac{\bar{T}_w - \bar{T}_\delta}{\bar{u}_\delta^2/(2c_p)} - \frac{2Pr}{\bar{u}_\delta} \frac{\bar{q}_{yw}}{\bar{\tau}_w} \tag{4.38}$$

Finally, the relationship between temperature and density is given by the ideal gas equation:

$$p = \rho R T \tag{4.39}$$

Accounting for density variation is fundamental for applying the Van Driest compressibility transformation.

4.4 Calculation procedure

This section explains the procedure the algorithm uses to implement the wall model starting from the values at the matching location.

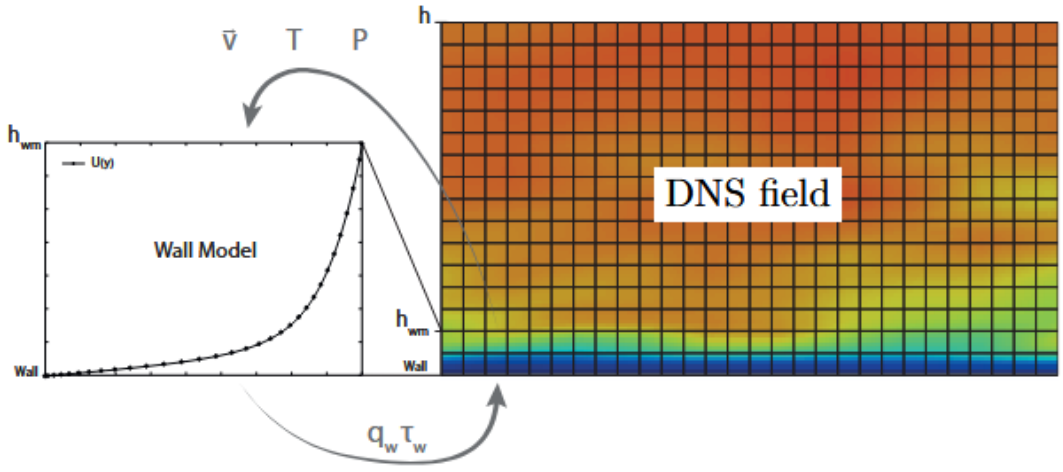

Figure 24: Concept of the procedure for calculating the heat transfer and skin friction at the wall. Starting from DNS data at a certain matching location h_{wm}, the model determines the velocity and temperature profiles inside a region with smaller spatial discretization.

The steps to implement the sheltering model are as follows:

1. An initial guess of u_τ/U_h (e.g. 0.1) is used to evaluate the wake expansion rate $\tan(\theta)$.
2. Calculate the sheltering height h_s.
3. Use 4.16 to obtain the attenuation factor.
4. Evaluate d and z_0 using 4.10 and 4.11.
5. Obtain the corrected u_τ/U_h with 4.7 and iterate until convergence.

At the end of this process, an initial guess of u_τ and T_τ is chosen and the differential logarithmic layer is integrated from h up to the matching location y_{ml}. The convergence of u_τ is verified by the equivalence of the integrated velocity profile at y_{ml} with the u_{ml} from DNS. During every iteration, the temperature is calculated from equation 4.37. In this work, different methods are presented to calculate the value of T_τ (and q_w).

- The first utilizes a quadratic relationship between velocity and temperature (Zhang et al., 2014):

$$T = b_0 + b_1 u + b_2 \frac{u^2}{2} \tag{4.40}$$

The coefficient b_0, b_1 and b_2 are obtain from the constraints that impose the the temperature to be zero at the wall $T(u = 0) = T_w$, and to correspond at the DNS values at the matching location and at the edge of the boundary layer ($T(u = u_{ml}) = T_{ml}$ and $T(u = u_\infty) = T_\infty$. Applying these conditions to 4.40 gives:

$$b_0 = T_w \tag{4.41a}$$

$$T_{ml} = T_w + b_1 u_{ml} + b_2 \frac{u_{ml}^2}{2} \tag{4.41b}$$

$$T_\delta = T_w + b_1 u_\delta + b_2 \frac{u_\delta^2}{2} \tag{4.41c}$$

Since $T_{ml}, u_{ml}, T_\delta, u_\delta$ are known values, equations 4.41b and 4.41c become a system of two equations in two unknowns b_1 and b_2. Once the coefficients are deduced, it is possible to use equation 4.40 to find the temperature T_h using U_h. During the integration of the log-layer, the value of the velocity at every point is used to compute the temperature using 4.40. After the integration process, the heat transfer is computed knowing that $q_w = T_\tau c_p \rho_w u_\tau$ (that is the definition of the friction temperature 3.40), than the generalised recovery factor r_g is obtained by 4.38 and the friction temperature come from using the value of T_h in equation 4.37 so it becomes:

$$T_\tau = \left(T_h - T_w + r_g \frac{U_h^2}{2c_p} \right) \frac{U_h}{u_\tau Pr} \tag{4.42}$$

- The second way is also based on knowing the values of velocity and temperature at the edge and at the matching location. The firsts are used to calculate the generalised recovery factor r_g with 4.38 and the seconds to evaluate T_τ using 4.37. The main difference is that this method is based solely on equation 4.37 to estimate the temperature profile and does not require the quadratic relationship 4.40 to initially determine the value of T_h.

- Finally, the last strategy is to use only the values in the matching location for r_g and T_τ. The temperature profile is derived from the velocity one by using equation 4.37. This method could even use only the values at the edge of the boundary layer if necessary, but it require an additional equation:

$$q_w = \left(u_{ml}\tau_w + c_p \frac{\mu_{t,wm}}{Pr_{t,wm}} \frac{\partial T}{\partial y} \right)_{y=y_{ml}} \tag{4.43}$$

This is the result of the vertical integration of the energy equation (Yang et al., 2018):

$$\frac{d}{dy}\left[(\mu + \mu_{t,\mathrm{wm}})\, u \frac{du}{dy} + c_p \left(\frac{\mu}{Pr} + \frac{\mu_{t,\mathrm{wm}}}{Pr_{t,\mathrm{wm}}} \right) \frac{dT}{dy} \right] = 0 \tag{4.44}$$

where $\mu_{t,wm} = \tau_w/(du/dy)$ and $Pr_{t,wm} = 0.9$.

5. Results

5.1 Simulation setup

The analysis revolves around a direct numerical simulation (DNS) of a supersonic, zero-pressure gradient, adiabatic, turbulent boundary layer at a free-stream Mach number of $M_\infty = 2$, over cubical, aligned roughness elements, performed by Cogo et al., 2025.The simulation was very expensive from a computational point of view and was performed with STREAmS (Bernardini et al., 2021), an open source software oriented to modern High-Performance-Computing (HPC) platforms using Message-Passing-Interface (MPI) parallelization and supporting multi-GPU architectures, that solves the Navier-Stokes equations for a viscous, heat-conducting gas. Resources for one simulation consisted of 64 nodes with 4 x GPUs/node (256 GPUs in total) for a domain discretised with 16 billion nodes and it was computed by the Leonardo cluster at CINECA. The simulations feature turbulent flow transitioning from a smooth to a rough surface with an extended computational domain to facilitate recovery. The methodology consisted in solving the compressible Navier–Stokes equations for a viscous, heat-conducting gas. The molecular viscosity μ is assumed to follow Sutherland's law, with a reference free-stream temperature $T_\infty = 220\ K$. The thermal conductivity k is related to the viscosity through the Prandtl number $Pr = 0.72$, $k = \frac{\mu c_p}{Pr}$, where c_p is the specific heat at constant pressure. The system of equations is completed by the equation of state for a calorically perfect gas and is solved on a Cartesian grid using the in-house code STREAmS (Bernardini et al., 2021), which has been extensively validated in numerous canonical flow configurations.

The rough-wall simulations consist of three regions: an initial smooth-wall part dedicated to the development of a turbulent boundary layer, obtained through a recycling/rescaling procedure, where the recycling plane is placed at $x = 40\delta_{in}$ (δ_{in} is the boundary layer thickness at the inflow). The second part starts at $x = 55\delta_{in}$, ends at $x = 147\delta_{in}$ and consists of cubic elements of side k, which are representative of the structured roughness patterns forming over ablative surfaces. Finally, a small smooth-wall part is placed at the end of the domain until $x = 150\delta_{in}$ as a buffer region before the outflow. In the smooth section the location of the recycling/rescaling procedure is placed at $x = 40\delta_{in}$ to achieve a fully developed turbulent boundary layer before the onset of roughness, followed by an additional $15\delta_{in}$ units as a buffer region to avoid any upstream influence of roughness on the recycling plane. The rough portion is extended as far as possible in order to adequately study the boundary layer adjustment to the new surface, but it transitions back to a smooth one $3\delta_{in}$ units before the outflow (hence up to $147\delta_{in}$) to not interfere with the boundary conditions. The roughness elements are spaced by a distance $2k$ in the wall-parallel directions, as shown in figure 25. The complexity of the geometry is handled using a ghost-point-forcing immersed boundary method, which is used to enforce no-slip adiabatic boundary conditions on the solid wall.

In figure 25(a), there is an overview of the instantaneous flow organisation to build a qualitative understanding of the main flow features. Before the roughness, a canonical smooth-wall organisation can be seen, which is abruptly disrupted by the occurrence of a shock wave caused by the first row of roughness elements. In the

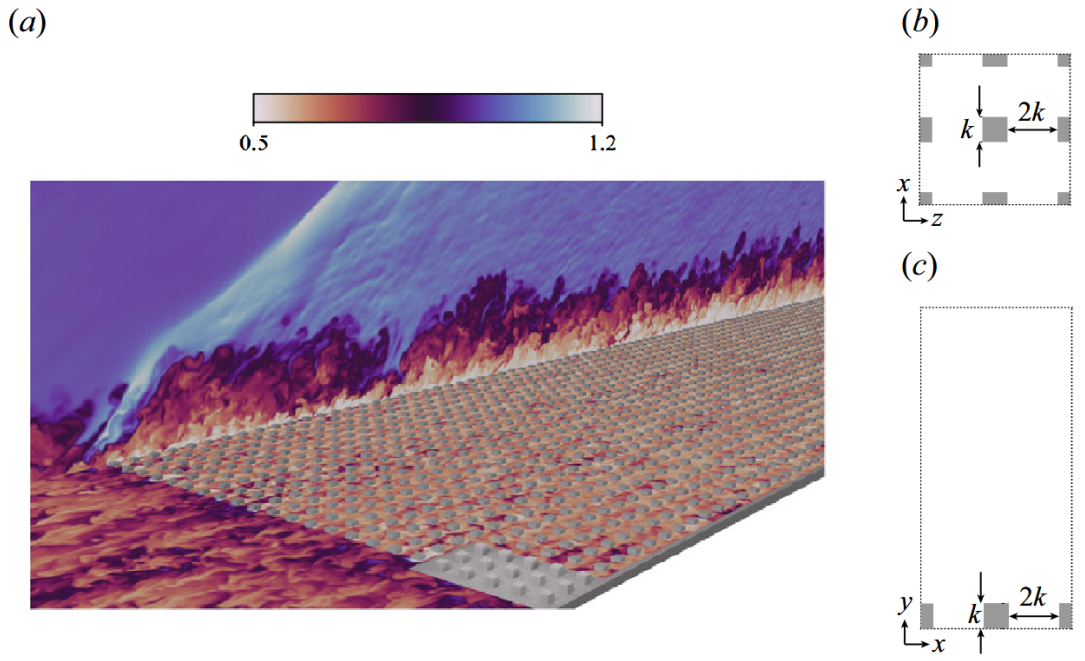

Figure 25: Schematic of the computational set-up for a turbulent boundary-layer flow over cubical roughness. (a) Instantaneous density field ρ/ρ_∞ of the DNS setup used for reference (the flow is subjected to a transition from a smooth to a rough surface to facilitate recovery) Cogo et al., 2025. (b) Wall-parallel arrangement of 3-D cubes in the rough portion. (c) Cross-stream arrangement of 3-D cubes. The roughness elements have height k and spacing $2k$ (Cogo et al., 2025).

longitudinal plane, behind the shock wave, a series of expansion and compression waves can be observed, possibly caused by the roughness pattern below. At the smooth-to-rough transition, the authors compared the development of an internal boundary layer between the subsonic and supersonic cases. Turbulence statistics are then evaluated far from the surface transition, where various compressibility transformations reveal the validity of the outer-layer similarity for the mean velocity. Analysis of thermal statistics for the supersonic case confirms the significant influence that roughness has on both mean and fluctuating temperature fields, which, unlike velocity fields, do not display outer layer similarity.

5.2 Qualitative results

5.2.1 Aligned cubical elements

Figure 26 shows the averaged stream-wise velocity obtained from DNS. A region of flow characterised by low momentum develops downstream of every element, as predicted by the sheltering mechanism of figure 21. The sheltered height h_s is visibly greater than zero, so the exponential profile is expected to have an attenuation coefficient $a > a_{min}$. The value of the frontal solidity for the case considered is $\lambda_f = 1/9$, while the roughness height (and width) is $k = 0.12\delta_{in}$. The distance between the elements, both stream-wise and span-wise is $2k$. It is worth noticing

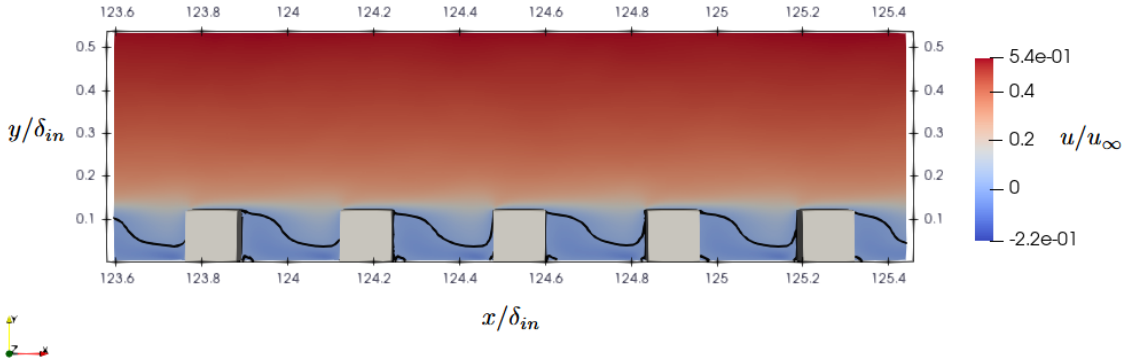

Figure 26: Contour of mean stream-wise velocity for aligned cubical elements. Flow goes from left to right. In the roughness sub-layer, the concept of sheltering mechanism can be noted by the wake being eaten up vertically, as sketched by the the black iso-line traced for $u/u_\infty = 0$.

that the velocity also assumes negative values in some region of the roughness sub-layer.

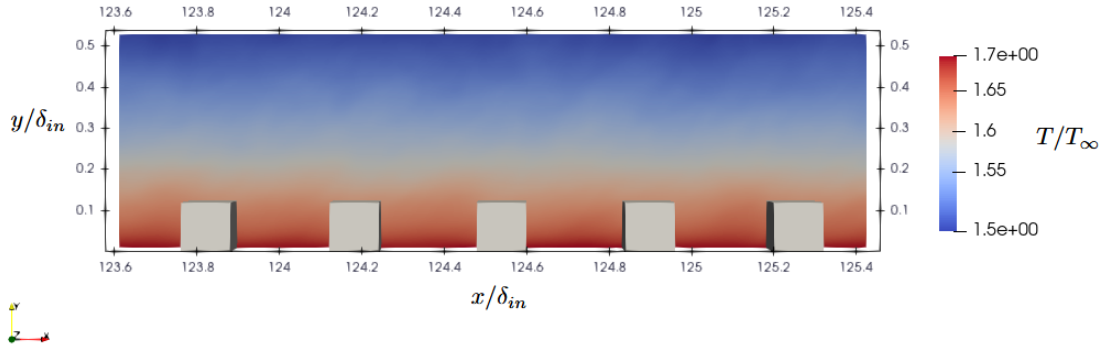

Figure 27: Contour of temperature for aligned cubical elements. Flow goes from left to right. In the roughness sublayer, the temperature is substantially at stagnation conditions, as well as the density because of the ideal gas law.

The flow in the roughness sublayer can be considered at stagnation condition, so the temperature and density are basically constant and uniform throughout this region. Therefore, the assumption that the roughness sublayer is treated as an incompressible flow is acceptable, and there is no necessity to adopt a compressible transformation even for the exponential velocity profile. Figure 27 shows the temperature contour for the case of the adiabatic wall, for which the ratio between the temperature at the wall and at free stream condition is approximately $T_w/T_\infty \simeq 1.7$.

The present model also takes into account the sheltering mechanism in the spanwise direction (23), but this is not the case for aligned cubical elements, as figure 28 shows. The wake projection is very similar to the one shown in figure 22

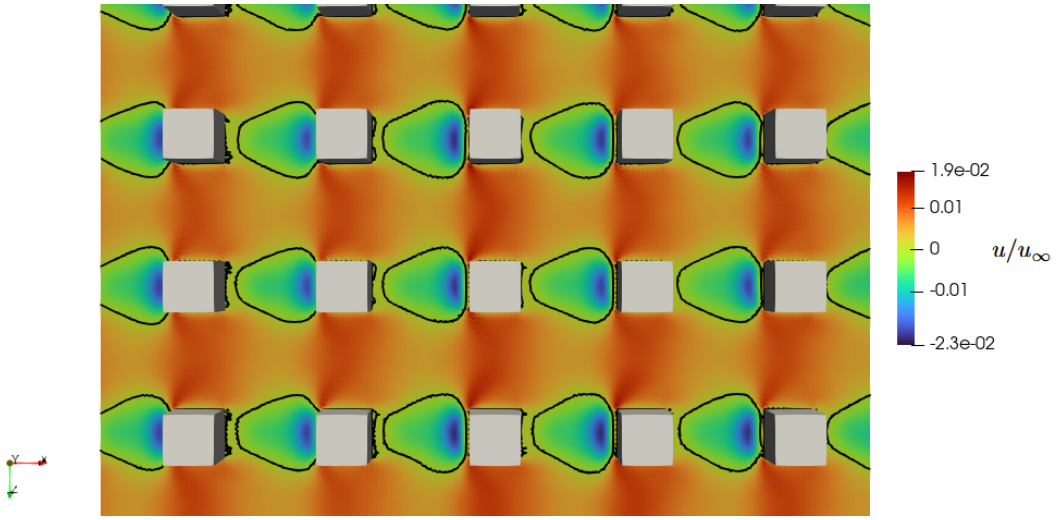

Figure 28: Contour of mean stream-wise velocity near the wall ($y/\delta_{in} = 0.001$). Behind every cube, the wake projection is identified by the black iso-line traced for $u/u_\infty = 0$.

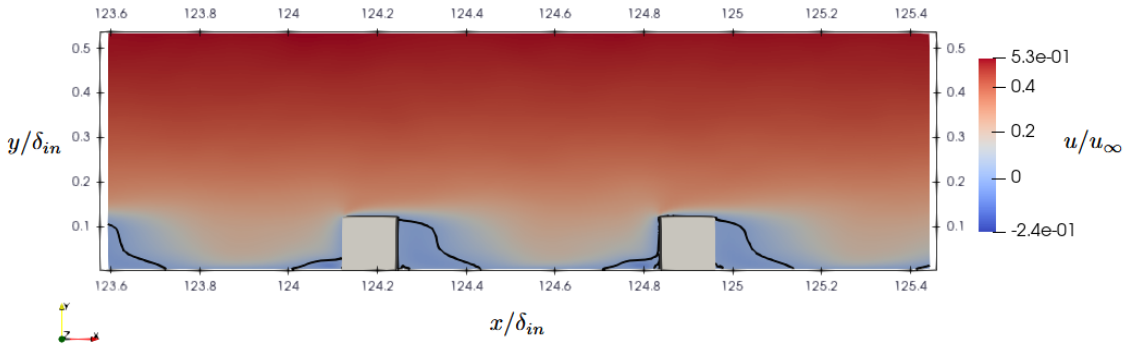

Figure 29: Contour of stream-wise velocity for aligned cubical elements. In the roughness sub-layer, the concept of sheltering mechanism can be noted by the wake being eaten up vertically.

5.2.2 Staggered cubical elements

In figure 29 it looks like the sheltering mechanism is not present since the downstream element is too far away. In other terms, the height h_{B_1A} in figure 23 shall be zero. However, the same cannot be said for the sheltering caused by the staggered elements (B_2 and B_3 in figure 23).

The temperature and density distribution are uniform below the roughness crests; therefore, even for the staggered case the hypothesis of incompressible fluid in the roughness sublayer persists.

For what concerns the wake development behind the staggered elements, figure 31 shows that the staggered elements (B_2 and B_3 in figure 23) have an influence on the downstream element. This means that the sheltered height h_{B_2A} and width w_2 are not zero, which leads to the attenuation constant being a little greater than a_{min}.

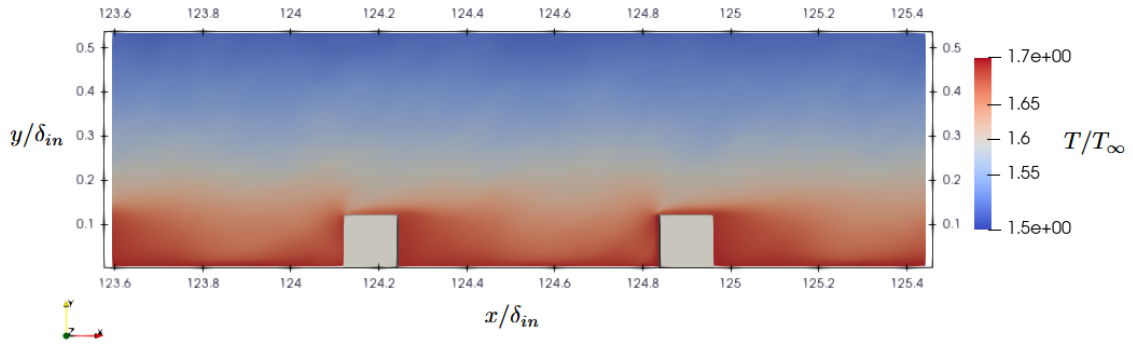

Figure 30: Contour of temperature for staggered cubical elements. The same conclusions stated for the aligned elements applies here.

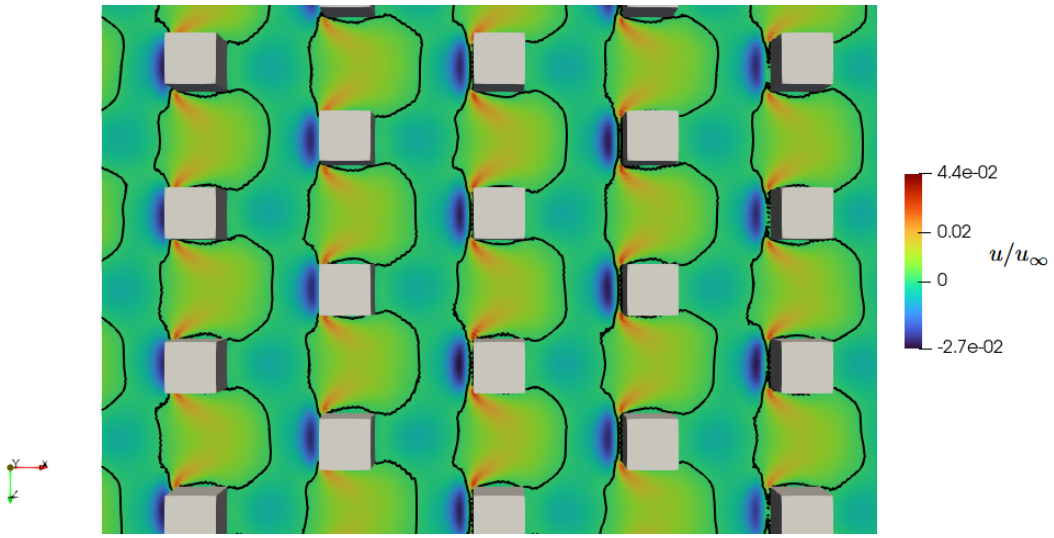

Figure 31: Contour of stream-wise velocity for staggered cubical elements. Even if two consecutive elements do not shelter each other, the same thing can't be said for wake developing behind the staggered ones.

5.3 Quantitative results

5.3.1 Two matching location model for aligned cubical elements

Figure 32 shows the results of the first model in predicting the velocity and temperature profiles of the adiabatic and isothermal boundary layer over aligned cubical elements. The scaled velocity profile is useful to evaluate the friction velocity u_τ and consequently the skin friction τ_w. For this reason, the obtained profiles do not necessarily pass through the matching data if the predicted wall stress is inaccurate. The matching location is set at $y^+ = 400$, which is almost the limit of validity of the log law for a simulation at $Re_\tau \simeq 1700$.

The relative error in the prediction of wall stress ϵ_{τ_w} is defined as:

$$\epsilon_{\tau_w} = \frac{\tau_{w,DNS} - \tau_{w,model}}{\tau_{w,DNS}} \cdot 100\% \tag{5.1}$$

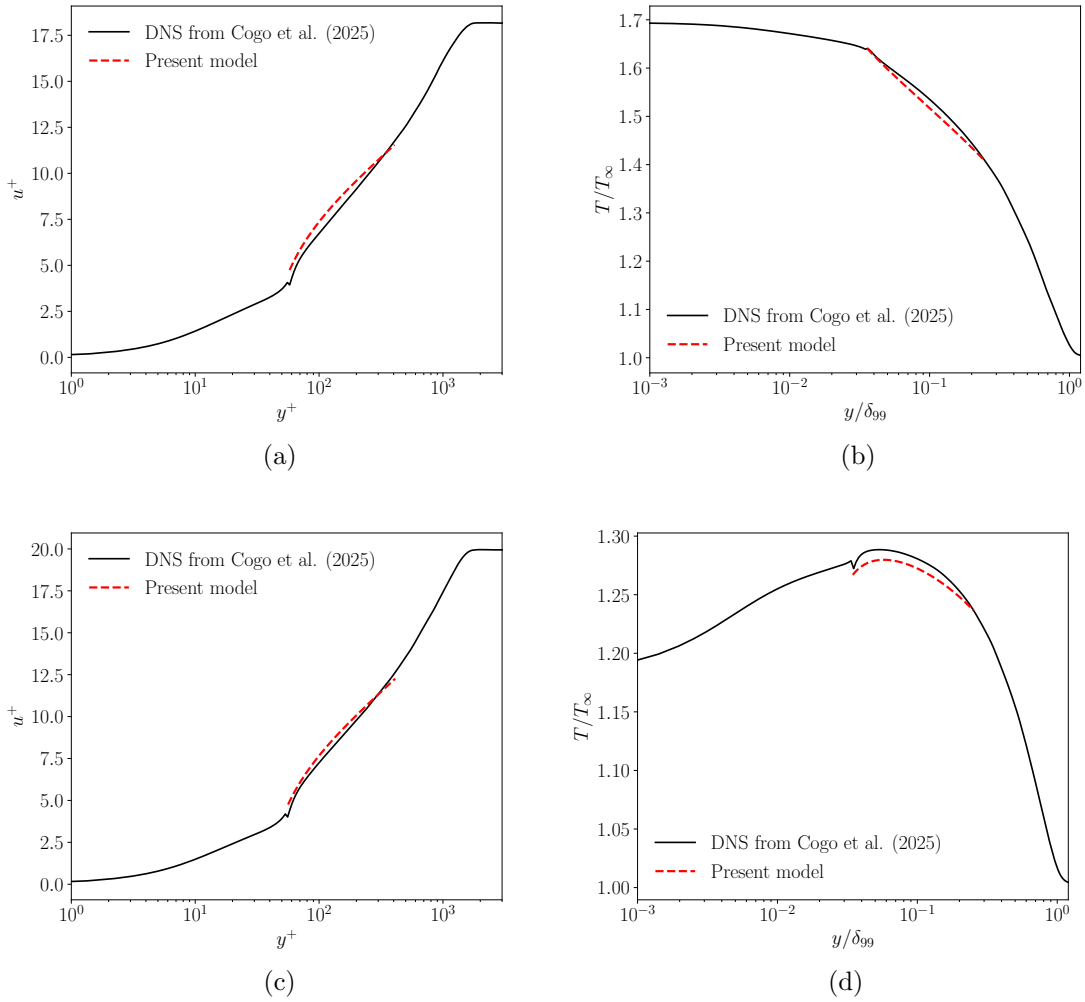

Figure 32: Scaled velocity and temperature profile estimated by the first model compared with DNS data from Cogo et al., 2025. The curves are shown only from the roughness crest up to the matching location. (a) and (b) refers to the adiabatic wall case with $T_w/T_\infty = 1.7$, while (c) and (d) to the isothermal one with $T_w/T_{aw} = 0.7$.

and the relative error in the wall heat flux is defined as

$$\epsilon_{q_w} = \frac{q_{w,DNS} - q_{w,model}}{q_{w,DNS}} \cdot 100\% \tag{5.2}$$

Here, ϵ_{q_w} is not reported for adiabatic boundary layer data because it is undefined, and both models predict negligible heat transfer for these data.

Both figure 32 and table 1 show good agreement between DNS data and the model. By adopting the quadratic relationship 4.40 for the estimation of T_h, the prediction of q_w is considerably better. In summary, the sheltering mechanism explained by Yang et al., 2016 represents a good approximation of the behaviour of the fluid in the roughness sub-layer. Due to the hypothesis of negligible compressibility effects in this region, the exponential layer supplies the differential logarithmic layer with a valid value of U_h (since the continuity between the two profiles is imposed)

Model 1	ϵ_{τ_w}	ϵ_{q_w}
Adiabatic	2.6%	-
Isothermal	4.5%	3.4%

Table 1: Estimated errors committed by the first model. The value for the adiabatic case is not reported because q_w is zero.

from which the integration starts. Then, the logarithmic layer accounts for density variation and adjusts the value of u_τ until the velocity is achieved at the matching location.

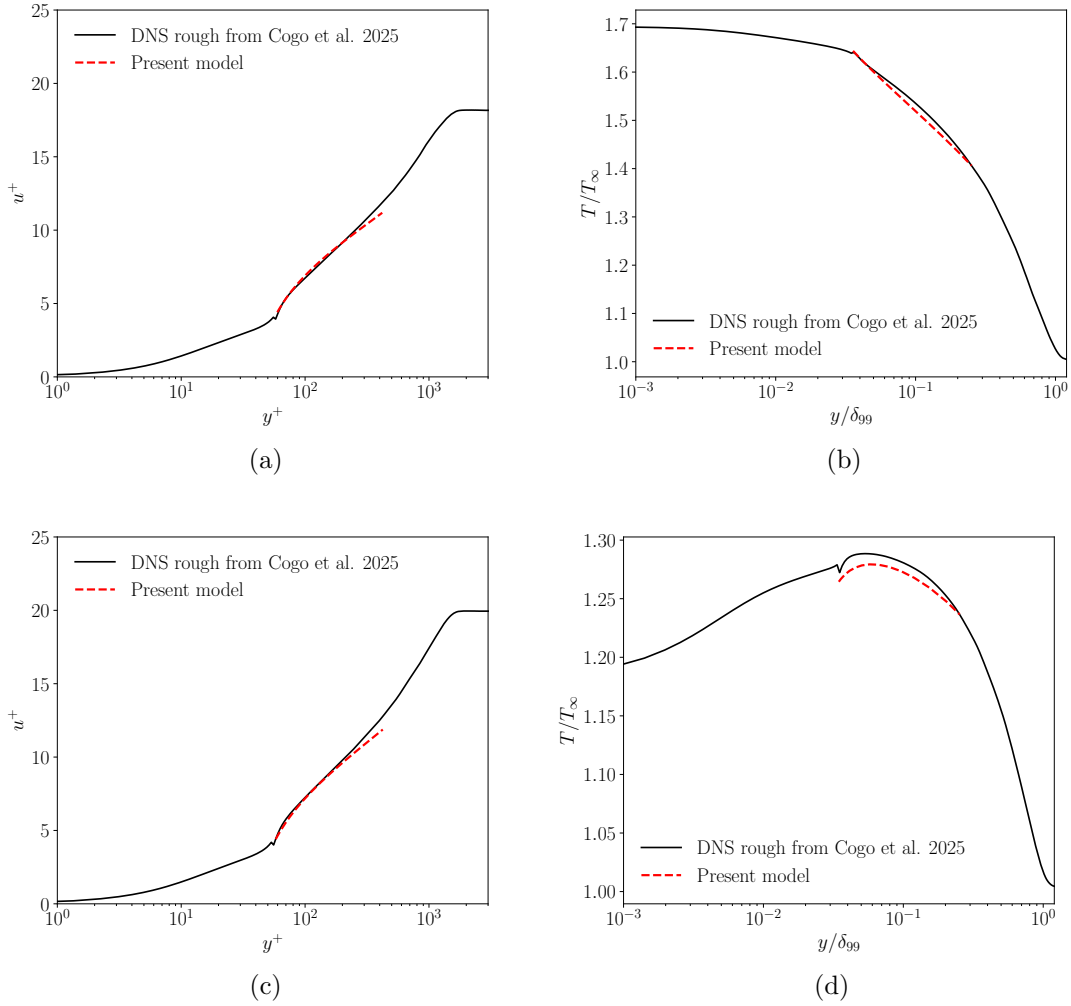

Figure 33: Scaled velocity and temperature profile estimated by the second model compared with DNS data from Cogo et al., 2025. The curves are shown only from the roughness crest up to the matching location. (a) and (b) refers to the adiabatic wall case, while (c) and (d) to the isothermal one.

Figure 33 refers to the second evaluation strategy of T_τ and q_w during each iteration. This approach does not implement the quadratic function 4.40 and therefore only uses the values of $T_{ml}, T_\infty, u_{ml}, u_\infty$ to calculate r_g and T_τ. The curve is then plotted down to $y = h$ using 4.37.

Model 2	ϵ_{τ_w}	ϵ_{q_w}
Adiabatic	9.4%	-
Isothermal	11.3%	38.9%

Table 2: Estimated errors committed by the second model. The value for the adiabatic case is not reported because q_w is negligible.

Table 2 shows that this model has a lower precision in estimating skin friction and heat transfer, but does not relate to a temperature value close to the wall. The

first model uses T_h to calculate T_τ, but since equation 4.31 shall work only at a certain distance from the wall. In summary, the first model extends the validity of the generalised Reynolds analogy to $y = h$, but this is not verified in general for rough surfaces, while the second model does not require this hypothesis.

5.3.2 One matching location model for aligned cubical elements

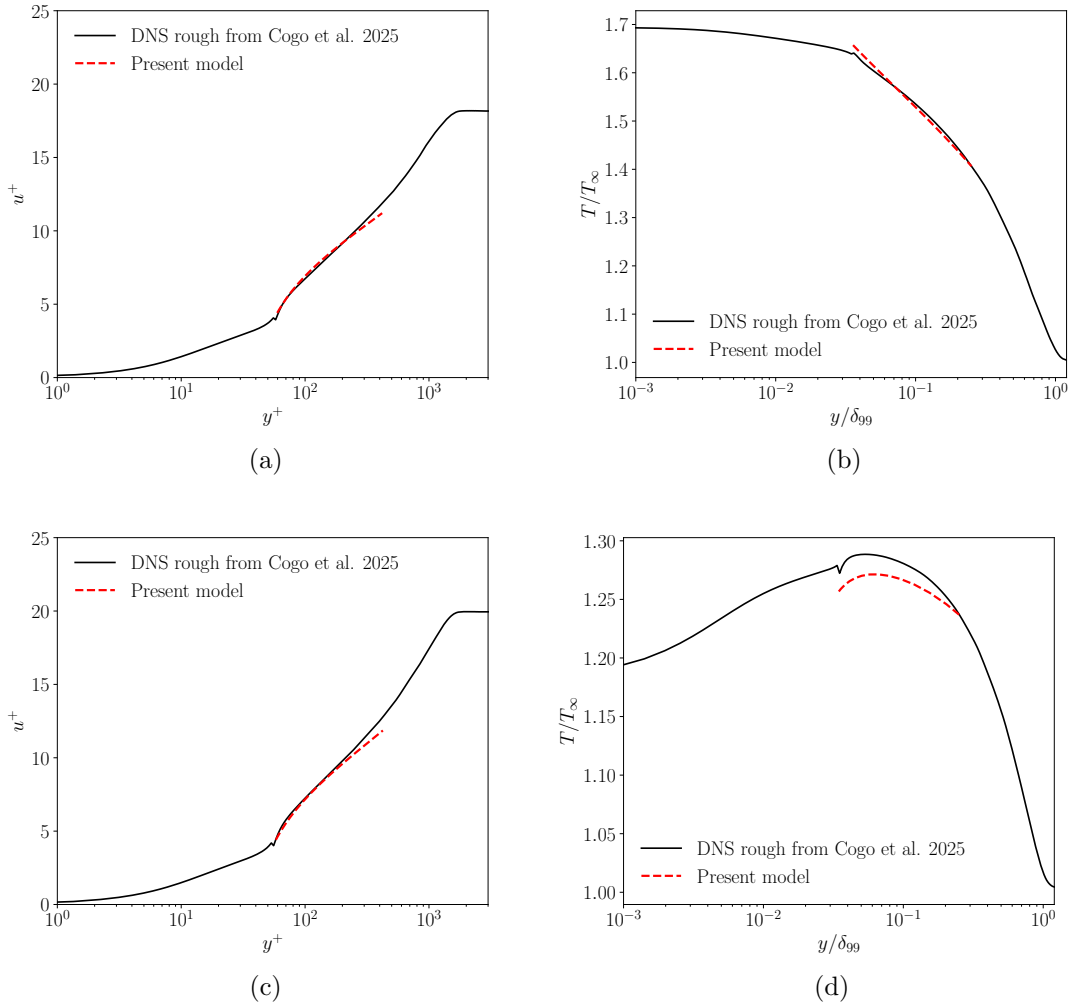

Figure 34: Scaled velocity and temperature profile estimated by the third model compared with DNS data from Cogo et al., 2025. The curves are shown only from the roughness crest up to the matching location. (a) and (b) refers to the adiabatic wall case, while (c) and (d) to the isothermal one.

The last approach is to evaluate both r_g and T_τ using only u_{ml} and T_{ml}. Then q_w is calculated by mean of 4.43. Results are shown in 34. While the error on u_τ (and τ_w) can be perceived by the fact that the two profiles of scaled velocity do not coincide at the matching location, the error on T_τ (and q_w) cannot be observed by looking at the temperature graph. This model could be useful whenever a single data point is available; it could also use the values at the edge, but the errors are expected

to increase because the wake correction does not take compressibility effects into account. In the future, other compressible transformations will be tested, such as the one by Hasan et al., 2024. Another problem of this model comes from equation 4.43 that only predicts the effect of the additive aerodynamic heating caused by roughness, but not the increase in heat transfer due to change in surface area.

Model 3	ϵ_{τ_w}	ϵ_{q_w}
Adiabatic	9%	-
Isothermal	11.7%	25.3%

Table 3: Estimated errors committed by the third model. The value for the adiabatic case is not reported because q_w is negligible.

5.3.3 Two matching location model for staggered cubical elements

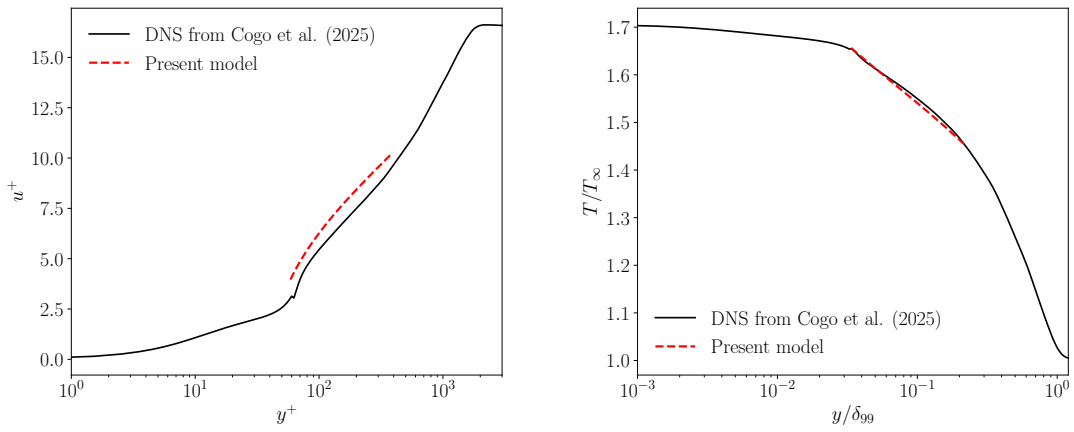

(a) (b)

Figure 35: Scaled velocity and temperature profile estimated by the first model compared with DNS data from Cogo et al., 2025 for staggered cubical elements. The curves are shown only from the roughness crest up to the matching location. (a) and (b) refers to the adiabatic wall case.

The last case studied in this work is the adiabatic surface with staggered cubical elements. The results of figure 35 show that the sheltering mechanism also works for this type of texture. The error in the prediction of skin friction in $\epsilon_{\tau_w} = 9.7\%$. As mentioned in the previous subsection, even if the height h_{B_1A} is zero, the other parameters h_{B_2A} and w_2 are a little greater than zero. So, the attenuation coefficient assumes a value of $a = 0.42$, which is barely higher than the minimum, leading to a small sheltering effect.

5.3.4 Hill correlation

In conclusion, it is important to compare the results obtained by the isothermal temperature models described before with an empirical correlation, like the one proposed by Hill, 1980 for hypersonic flows. The correlation is expressed as a ratio between the Stanton numbers for rough and smooth walls:

$$\frac{St}{St_s} = \frac{Cf}{Cf_s}\left[1 + \beta\sqrt{\frac{T_w}{T_b}\frac{Cf}{2}} + k^{+0.45}Pr^{0.8}\right]^{-1} \tag{5.3}$$

where St is the Stanton number (the s subscript stands for smooth) and Cf is the friction coefficient. The temperature profile is obtained from equation 4.40 where $b_0 = T_w$, b_2 comes from the equivalence at the matching location and b_1 comes from the first derivative of 4.40 evaluated at the wall.

$$b_1 = \left.\frac{dT}{dU}\right|_w = s\frac{T_r - T_w}{u_\infty}Pr \tag{5.4}$$

where

$$s = 2\frac{St}{Cf} \tag{5.5}$$

is the Reynolds analogy factor. The Stanton number is obtained from the Hill correlation 5.3 after calculating the rough friction coefficient $Cf = 2\tau_w/(\rho_\delta u_\delta^2)$, and then the Reynolds analogy factor can be computed. The results are reasonable in terms of skin friction (only $\epsilon_{\tau_w} = 4.5\%$) but are not acceptable for what concerns heat transfer $\epsilon_{q_w} = 153\%$

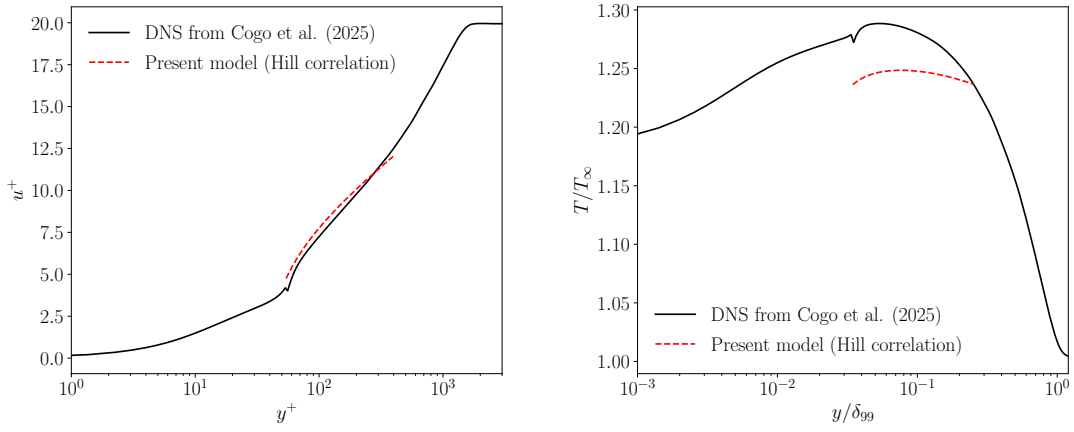

(a) (b)

Figure 36: Scaled velocity and temperature profile estimated by the first model compared with DNS data from Cogo et al., 2025 for aligned cubical elements. The curves are shown only from the roughness crest up to the matching location. (a) and (b) refers to the isothermal wall case.

6. Conclusions

Compressible wall-bounded turbulent flows are ubiquitous on the surfaces of high-speed flying vehicles, gas turbine blades, rocket motor nozzles, etc. In these flows, heat transfer is as important as aerodynamic force. For the structure to be safe, efficient, reliable and economical, an accurate estimation of the velocity and thermal fields is needed, which is difficult because of the roughness presence on the surfaces. The purpose of the model presented in this thesis is to provide a tool that can predict the evolution of fluid dynamics within a compressible rough boundary layer, starting from a point called matching location. This allows one to evaluate the effects of roughness topography on the main variables of the flow without performing heavy and expensive DNS. The model proposed by Yang et al., 2016 is here extended in the compressible regime and a compressible transformation (Van Driest, 1951) has been implemented to account for density variations through the logarithmic layer. The results show a good agreement with the data from simulations regarding a supersonic, turbulent boundary layer over cubical, aligned roughness elements. The error in the prediction of τ_w is 2.6% for the adiabatic wall and 4.5% for the isothermal wall. The temperature profile is obtained using the generalised Reynolds analogy proposed by Zhang et al., 2014. It is a concept based on the similarity between the momentum and energy equations from which a quadratic relationship between temperature and velocity is derived. The coefficient of such relationship comes from the application of the constraints at the wall, matching location and boundary layer edge and is used to estimate the value of the temperature at the roughness crest T_h. As expected, the model calculates a negligible heat transfer for the adiabatic case, while committing a low error in the estimation of q_w for the isothermal case (only 3.4%). Other two temperature-velocity relations have been implemented in this work. The first uses the values of velocity and temperature at matching location and at the $y = \delta$ to determine the values of the generalised recovery factor r_g and friction temperature T_τ, without first estimating the value of T_h like in the previous strategy. The errors in this way are higher for both skin friction and heat transfer ($\epsilon_{\tau_w} = 9.4\%$ for the adiabatic case and $\epsilon_{\tau_w} = 11.3\%$ and $\epsilon_{q_w} = 38.9\%$ for the isothermal). The final method only employs the DNS value at the matching location to estimate r_g and T_τ and utilizes an additional equation obtained by the vertical integration of the RANS energy equation. The errors this time are $\epsilon_{\tau_w} = 9\%$ for the adiabatic case and $\epsilon_{\tau_w} = 11.7\%$ and $\epsilon_{q_w} = 25.3\%$ for the isothermal case. The model currently works also for cubical, staggered elements, for which the sheltering mechanism still applies. In conclusion, the results have been compared with an existing correlation proposed by Hill, 1980, the error is not acceptable for what concerns heat transfer in the isothermal case ($\epsilon_{q_w} = 153\%$).

In the future, the model will be tested for new geometries and with other compressible transformations like the one from Hasan et al., 2024. More importantly, hypersonic flows need to be tested as experimental and numerical reference data become available in the future. In this case, the velocity below the boundary layer is much higher, and every roughness element has the potential to generate a shock wave, so the model should be modified to account for this type of phenomenon.

Because pyrolysis is a non-uniform process driven by the local dynamics of the

flow, it is also foreseen to generate a filtered random Gaussian roughness distribution that better represents a realistic topography of an ablated surface.

After testing the model with various new data and geometry, the next step is to combine it with a full-scale simulation code for a re-entry capsule. A Large-Eddy-Simulation (LES) utilises a model that represents the small-scale turbulent eddies (which are not directly resolved). A modified version called Wall-Modelled Large Eddy Simulation (WMLES) has gained popularity in recent years because of its property of capturing the non-stationary nature of the main flow and the model developed in this work can describe the parameters of interest in the near-wall portion.

A. Appendix - Navier-Stokes equations

The entirety of fluid mechanics is described by the Navier-Stokes equations, which express momentum balance, conservation of mass and energy for Newtonian fluids.

A.1 Divergence theorem

Taken a closed volume v (fig. 37), the divergence theorem states:

$$\int_{\partial v} \mathbf{F} \cdot \hat{n} dS = \int_{v} \vec{\nabla} \cdot \mathbf{F} dv \tag{A.1}$$

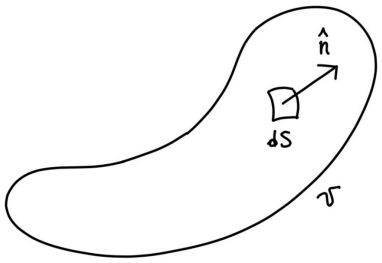

Figure 37: Example of a control volume with v a frontier ∂v and a normal $\hat{n}$

where $\mathbf{F}$ is a tensor of at least first order and $\hat{n}$ is the normal to the surface.

A.2 Reynolds transport theorem

Consider a system of fluid particles in the volume v_s, changing over time, so that $v_s(t) \neq v_s(t + dt)$. Given a certain extensive quantity $\mathbf{B}$ (that can be a function of both space and time) and the corresponding intensive quantity $\mathbf{b}$ the Reynolds transport theorem states that:

$$\frac{d}{dt}\mathbf{B} = \frac{d}{dt}\int_{v_s(t)} \rho \mathbf{b} dv = \frac{d}{dt}\int_{v_c} \rho \mathbf{b} dv + \int_{\partial v_c} \rho \mathbf{b} \vec{V} \cdot \hat{n} dS \tag{A.2}$$

This theorem allows to build a relationship between a physical law and the control volume v_c which is fixed over time, by adding a flux term that takes into account the quantities going in and out the frontiers.

A.3 Mass conservation equation

The law of conservation of mass states that the time variation of mass in a system has to be zero:

$$\frac{d}{dt} m_s = 0, \quad where \quad m_s = \int_{v_s(t)} \rho dv \tag{A.3}$$

Using the Reynolds transport theorem A.2:

$$\frac{d}{dt}m_s = 0 = \frac{d}{dt}\int_{v_s(t)} \rho dv = \frac{d}{dt}\int_{v_c} \rho dv \ + \int_{\partial v_c} \rho \vec{V} \cdot \hat{n} dS \tag{A.4}$$

Than applying the divergence theorem A.1 and taking the time derivative inside the integral sign because v_c is time independent:

$$\int_{v_c} \frac{\partial \rho}{\partial t} dv \ + \int_{\partial v_c} \vec{\nabla} \cdot (\rho \vec{V}) dv = \int_{v_c} \left[\frac{\partial \rho}{\partial t} + \vec{\nabla} \cdot (\rho \vec{V}) \right] dv = 0 \tag{A.5}$$

Since the latter expression is valid for every control volume v_c, the integral sign can be omitted and the conservative form of the mass balance equation is obtained as follow:

$$\frac{\partial \rho}{\partial t} + \vec{\nabla} \cdot (\rho \vec{V}) = 0 \tag{A.6}$$

A.4 Momentum conservation

Newton's second law of motion sets off that the net force $\vec{F_e}$ on a body is equal to the rate at which the system's momentum $\vec{Q_s}$ is changing with time:

$$\frac{d}{dt}\vec{Q_s} = \vec{F_e}, \quad where \quad \vec{Q_s} = \int_{v_s(t)} \rho \vec{V} dv \tag{A.7}$$

Again applying the A.2:

$$\frac{d}{dt}\vec{Q_s} = \frac{d}{dt}\int_{v_s(t)} \rho \vec{V} dv = \frac{d}{dt}\int_{v_c} \rho \vec{V} dv \ + \int_{\partial v_c} \rho \vec{V} \vec{V} \cdot \hat{n} dS = \vec{F_{e,v}} \ + \vec{F_{e,s}} \tag{A.8}$$

where the external forces has been divided in volume forces and surface forces:

$$\vec{F_e} = \begin{cases} d\vec{F}_{e,v} = \rho \vec{f} dv \\ d\vec{F}_{e,s} = \vec{t}_{(\hat{n})} dS = \vec{\vec{T}} \cdot \hat{n} dS \end{cases} \tag{A.9}$$

For Newtonian fluids, a constitutive relation between the stress tensor $\vec{\vec{T}}$ and the velocity gradient exists:

$$\vec{\vec{T}} = -p\vec{\vec{I}} + 2\mu\vec{\vec{E}} - \frac{2}{3}\mu(\vec{\nabla} \cdot u)\vec{\vec{I}} = -p\vec{\vec{I}} + \vec{\vec{\Sigma}} \tag{A.10}$$

where $\vec{\vec{I}}$ is the identity matrix, $\vec{\vec{E}} = \frac{1}{2}(\vec{\nabla}\vec{V} + \vec{\nabla}\vec{V}^T)$ is the deformation tensor, while $\vec{\vec{\Sigma}}$ is the viscous stress tensor.

Finally, using the divergence theorem A.1 and removing the integral sign, the conservative form of the momentum conservation equation is derived:

$$\frac{\partial \rho \vec{V}}{\partial t} + \vec{\nabla} \cdot (\rho \vec{V} \vec{V}) = \rho \vec{f} - \vec{\nabla} p + \vec{\nabla} \cdot \vec{\vec{\Sigma}} \tag{A.11}$$

A.5 Energy conservation

The first principle of thermodynamics states that a system increases or decreases its internal energy E_s (which includes also the kinetic energy) subsequentially to heat transfer Q or thermodynamic work transfer W. Here is shown the time derivative version of it:

$$\frac{d}{dt}E_s = \frac{d}{dt}\int_{v_s(t)} \rho\left(e + \frac{V^2}{2}\right)dv = \dot{Q}_v + \dot{Q}_s + \dot{W}_v + \dot{W}_s \tag{A.12}$$

where the heat and work contributes have been separated in volume and surface terms, using the Fourier law $\vec{q} = -k\vec{\nabla}T$:

$$d\dot{Q} = \begin{cases} d\dot{Q}_v = \rho\dot{Q}dv \\ d\dot{Q}_s = -\vec{q}\cdot\hat{n}dS = k\vec{\nabla}T\cdot\hat{n}dS \end{cases} \tag{A.13}$$

$$d\dot{W} = \begin{cases} d\dot{W}_v = \vec{V}\cdot(\rho\vec{f})dv = \rho\vec{V}\cdot\vec{f}dv \\ d\dot{W}_s = \vec{V}\cdot\vec{t}_{(\hat{n})}dS = \vec{V}\cdot\vec{\vec{T}}\cdot\hat{n}dS \end{cases} \tag{A.14}$$

Now, using the Reynolds transport theorem A.2, the divergence theorem A.1 and the constitutive equation A.5, the conservative form of the energy balance equation is derived:

$$\frac{\partial}{\partial t}\left[\rho\left(e + \frac{V^2}{2}\right)\right] + \vec{\nabla}\cdot\left[\rho\left(e + \frac{V^2}{2}\right)\vec{V}\right] = \rho\dot{Q} - \vec{\nabla}\cdot q - \vec{\nabla}\cdot(p\vec{V}) + \vec{\nabla}\cdot(\vec{V}\cdot\vec{\vec{\Sigma}}) + \rho\vec{V}\cdot\vec{f} \tag{A.15}$$

To condensate the right-hand terms, the notation of total derivative is introduced, so the final system will look like:

$$\frac{\partial\rho}{\partial t} + \vec{\nabla}\cdot(\rho\vec{V}) = 0 \tag{A.16a}$$

$$\frac{\partial\rho\vec{V}}{\partial t} + \vec{\nabla}\cdot(\rho\vec{V}\vec{V}) = \rho\vec{f} - \vec{\nabla}p + \vec{\nabla}\cdot\vec{\vec{\Sigma}} \tag{A.16b}$$

$$\rho\frac{Dh_0}{Dt} = -\frac{\partial p}{\partial t} + \vec{\nabla}\cdot(\vec{\nabla}\cdot\vec{\vec{\Sigma}}) + \vec{\nabla}\cdot(k\vec{\nabla}T) \tag{A.16c}$$

where $\rho, \vec{V}, T, p$, are the density, velocity, temperature and pressure fields respectively, while again $\vec{\vec{\Sigma}}$ is the viscous stress tensor, which, for Newtonian fluids, is written as:

$$\vec{\vec{\Sigma}} = \mu(\vec{\nabla}\vec{V} + \vec{\nabla}\vec{V}^T) - \frac{2}{3}\mu(\vec{\nabla}\cdot\vec{V})\vec{\vec{I}} \tag{A.17}$$

and h_0 is the specific total enthalpy, defined as:

$$h_0 = h + \frac{V^2}{2}. \tag{A.18}$$

For an ideal gas, the system A.16 is completed by the following equations:

$$p = \rho R T \tag{A.19a}$$
$$h = c_p T \tag{A.19b}$$
$$c_p = \frac{\gamma}{\gamma - 1} R \tag{A.19c}$$
$$\gamma = \frac{c_p}{c_v} \tag{A.19d}$$

while the viscosity μ follow the Sutherland law in order to take into account its variation with temperature:

$$\mu(T) = \mu_\infty \left(\frac{T}{T_\infty} \right)^{\frac{3}{2}} \frac{T_\infty + S}{T + S} \tag{A.20}$$

where $S_{air} = 110K$. Alternatively, a power law can be used to express the viscosity dependence on temperature:

$$\mu(T) = \mu_\infty \left(\frac{T}{T_\infty} \right)^{n} \tag{A.21}$$

where $n_{air} = \frac{2}{3}$.

A.6 Crocco-Busemann' first relation

From equations A.16, we can define a set of non-dimensional parameters, using quantities that describe a general aerodynamic problem: $\rho_\infty, U_\infty, p_\infty, \mu_\infty, k_\infty,$, are respectively the density, velocity, pressure, viscosity and thermal conductivity of the undisturbed flow at a certain distance from a body characterised by a dimension L_∞. By normalising the field quantities with respect to those just defined, we obtain a new set of equations in which three non-dimensional parameters appear:

- Mach number, $M = \frac{U_\infty}{\sqrt{\gamma R T_\infty}}$, which is an indicator of how much the kinetic energy fraction is, compared to the internal energy;
- Reynolds number, $Re = \frac{\rho_\infty U_\infty L_\infty}{\mu_\infty}$, which express the ratio between the inertial actions and the viscous terms;
- Prandtl number, $Pr = \frac{\mu_\infty c_p}{k_\infty}$, which expresses the ratio between kinematic and thermal diffusivities in a viscous fluid and, for air, the value is about $Pr_{air} = 0.71$.

By regrouping these terms, we obtain the non-dimensional Navier-Stokes equations, that are useful whenever an experiment needs to be performed in scale.

$$\frac{\partial \rho^*}{\partial t^*} + \vec{\nabla}^* \cdot (\rho^* \vec{V}^*) = 0 \tag{A.22a}$$
$$\rho^* \frac{D\vec{V}^*}{Dt^*} = -\frac{1}{\gamma M^2} \vec{\nabla}^* p^* + \frac{1}{Re} \vec{\nabla}^* \cdot \vec{\vec{\Sigma}}^* \tag{A.22b}$$
$$\rho^* \frac{Dh_0^*}{Dt^*} = -\frac{\partial p^*}{\partial t^*} + \frac{\gamma M^2}{Re} \vec{\nabla}^* \cdot (\vec{\nabla}^* \cdot \vec{\vec{\Sigma}}^*) + \frac{1}{RePr} \left(\frac{\gamma}{\gamma - 1} \right) \vec{\nabla}^* \cdot (k^* \vec{\nabla}^* T^*) \tag{A.22c}$$

The Reynolds number in most aerodynamic problems is extremely high, so we can separate the solution in external and internal (boundary layer) with a coordinate transformation and considering $\lim_{Re\to\infty}$, the Navier-Stokes equations become:

$$mass: \quad \frac{\partial \rho u}{\partial x} + \frac{\partial \rho v}{\partial y} \tag{A.23a}$$

$$momentum\ x: \quad \rho u\frac{\partial u}{\partial x} + \rho v\frac{\partial v}{\partial y} = -\frac{dP_{e,0}}{dx} + \frac{\partial}{\partial y}\left[\mu\frac{\partial u}{\partial y}\right] \tag{A.23b}$$

$$momentum\ y: \quad \frac{\partial p}{\partial y} = 0 \tag{A.23c}$$

$$energy: \quad \rho u\frac{\partial h_0}{\partial x} + \rho v\frac{\partial h_0}{\partial y} = \frac{\partial}{\partial y}\left(\mu u\frac{\partial u}{\partial y}\right) + \frac{\partial}{\partial y}\left(k\frac{\partial T}{\partial y}\right) \tag{A.23d}$$

where the left-hand term in the energy equation represents the transport of energy into the boundary layer (convective terms), while the right-hand terms represent the viscous and thermal diffusivity. It's worth noting that the total enthalpy h_0 can be expressed only in term of the stream-wise component of velocity.

$$h_0 = h + \frac{u^2}{2} \tag{A.24}$$

The viscous diffusivity term can be rewritten as:

$$\mu u\frac{\partial u}{\partial y} = \mu\frac{\partial}{\partial y}\left(\frac{u^2}{2}\right) \tag{A.25}$$

while the temperature can be expressed as a function of velocity following the constitutive equation A.5 (if $c_p = const$):

$$T = \frac{h}{c_p} = \frac{h_0}{c_p} - \frac{u^2}{2c_p} \tag{A.26}$$

so the thermal diffusivity term becomes:

$$k\frac{\partial T}{\partial y} = \frac{\mu}{Pr}\frac{\partial}{\partial y}\left(h_0 - \frac{u^2}{2}\right) \tag{A.27}$$

Substituting A.25 and A.27 in the energy equation of A.23 leads to the following:

$$\rho u\frac{\partial h_0}{\partial x} + \rho v\frac{\partial h_0}{\partial y} = \frac{\partial}{\partial y}\left(\mu\frac{\partial}{\partial y}\left(\frac{u^2}{2}\right)\right) + \frac{\partial}{\partial y}\left[\frac{\mu}{Pr}\frac{\partial}{\partial y}\left(h_0 - \frac{u^2}{2}\right)\right] \tag{A.28}$$

Rearranging the viscous and thermal diffusivity terms:

$$\rho u\frac{\partial h_0}{\partial x} + \rho v\frac{\partial h_0}{\partial y} = \frac{\partial}{\partial y}\left(\frac{\mu}{Pr}\frac{\partial}{\partial y}(h_0)\right) + \frac{\partial}{\partial y}\left[\left(1 - \frac{1}{Pr}\right)\mu\frac{\partial}{\partial y}\left(\frac{u^2}{2}\right)\right] \tag{A.29}$$

Assuming $Pr = 1$ the last term cancels itself out of the expression. The remaining equation has the solution $h_0 = const$ only if $\frac{\partial h_0}{\partial y} = 0$ at the edge and wall of the boundary layer. Forcing this condition on the wall is equivalent to setting the wall as adiabatic.

$$\left.\frac{\partial h_0}{\partial y}\right|_w = 0 \Leftrightarrow k\left.\frac{\partial T}{\partial y}\right|_w = 0 \tag{A.30}$$

Looking at equation A.29 and assuming:

- $Pr = 1$ (for gases $Pr \sim 1$, while for air $Pr = 0.72$;
- $q_w = 0$ (adiabatic wall);
- $c_p = const$;

the solution is $h_0 = const$ across the boundary layer. With this information, it is possible to derive the temperature profile:

$$T = T_0 + \frac{u^2}{2} \tag{A.31}$$

where the adiabatic wall temperature can be defined as $T_{aw} = T_0$ since the velocity is zero at the wall. Having $Pr = 1$ means that the flux of kinetic energy and thermal energy are balancing each other across the boundary layer.

A.7 RANS

The study of turbulent flows focuses on a statistical approach and in order to do so, averaging turns out to be a very useful mean. The Reynolds average is a type of mean value whose calculation is based on the number N of experiments:

$$U(x,t) = \langle u(x,t)\rangle = \frac{1}{N}\sum_{k=1}^{N>>1} u^{(k)}(x,t) \tag{A.32}$$

The mean quantities recover the symmetries of the boundary condition; therefore, if the experiment is performed at stationary regime, the Reynolds average coincides with the time average and $U(x,t) = U(x)$.

The Reynolds average operator is linear, so performing the derivative of the mean value is equivalent to calculating the average of the derivative.

A.7.1 Reynolds decomposition

Every quantity $u(x,t)$ can be expressed as a sum of its mean value $U(x,t)$ and a fluctuation from the mean value $u'(x,t)$:

$$u(x,t) = U(x,t) + u'(x,t) \tag{A.33}$$

by applying the Reynolds average to the decomposition above, it is simple to notice that the mean value of the fluctuation is zero $\langle u'\rangle = 0$.

Now, taking the Navier-Stokes equations

$$\frac{\partial u_j}{\partial x_j} = 0 \tag{A.34a}$$

$$\frac{\partial u_i}{\partial t} + \frac{\partial}{\partial x_j}(u_i u_j) = -\frac{1}{\rho}\frac{\partial p}{\partial x_i} + \frac{\partial}{\partial x_j}(2\nu e_{ij}) \tag{A.34b}$$

applying the decomposition $u_i = U_i + u_i'$ and averaging:

$$\vec{\nabla} \cdot \vec{U} \tag{A.35a}$$

$$\frac{\bar{D}\vec{U}}{D\bar{t}} = -\frac{\vec{\nabla} P}{\rho} + \vec{\nabla} \cdot (2\nu \vec{\vec{E}}) - \vec{\nabla} \cdot \langle \vec{u'} \vec{u'} \rangle \tag{A.35b}$$

where $\vec{\nabla} \cdot \langle \vec{u'} \vec{u'} \rangle$ is the **Reynolds stress tensor** and it is symmetric. System A.35 has four equations and ten unknowns (three components of mean velocity, the mean pressure and six components of the Reynolds stress tensor).

B. Bibliography

References

Van Driest, E. R. (1951). "Turbulent boundary layer in compressible fluids". In: *J. Aeronaut. Sci.* 18.3, pp. 145–160.

Goddard Jr, Frank E (1959). "Effect of uniformly distributed roughness on trubulent skin-friction drag at supersonic speeds". In: *Journal of the Aerospace Sciences* 26.1, pp. 1–15.

Reynolds, Osborne M. (1961). "On the extent and action of the heating surface of steam boilers". In: *International Journal of Heat and Mass Transfer* 3, pp. 163–166.

Morkovin, M. V. (1962). "Effects of compressibility on turbulent flows". In: *Mécanique de la Turbulence* 367.380, p. 26.

Walz, Alfred (1966). "Boundary layers of flow and temperature". In: *MIT Press*.

Hill, J. (1980). "Measurements of surface roughness effects on the heat transfer to slender cones at Mach 10". In: *AIAA*.

Townsend, AAR (1980). *The structure of turbulent shear flow*. Cambridge university press.

Raupach, M. R. et al. (1991). "Rough-Wall Turbulent Boundary Layers". eng. In: *Applied Mechanics Reviews* 44.1, pp. 1–25. ISSN: 0003-6900.

Latin, Robert M et al. (2000). "Flow properties of a supersonic turbulent boundary layer with wall roughness". In: *AIAA journal* 38.10, pp. 1804–1821.

Pope, Stephen B. (2000). *Turbulent Flows*. Cambridge University Press.

Jiménez, Javier (Jan. 2004). "Turbulent flows over rough walls". en. In: *Annu. Rev. Fluid Mech.* 36.1, pp. 173–196. ISSN: 0066-4189, 1545-4479. DOI: 10.1146/annurev.fluid.36.050802.122103.

Bowersox, Rodney (June 2007). "Survey of High-Speed Rough Wall Boundary Layers: Invited Presentation". en. In: *37th AIAA Fluid Dynamics Conference and Exhibit*. Miami, Florida: American Institute of Aeronautics and Astronautics. ISBN: 978-1-62410-008-6. DOI: 10.2514/6.2007-3998.

Ekoto, Isaac W et al. (2008). "Supersonic boundary layers with periodic surface roughness". In: *AIAA journal* 46.2, pp. 486–497.

Tyson, C. J. et al. (2013). "Numerical simulation of fully-developed compressible flows over wavy surfaces". In: *International Journal of Heat and Fluid Flow* 41, pp. 2–15. ISSN: 0142-727X. DOI: https://doi.org/10.1016/j.ijheatfluidflow.2013.02.006.

Zhang, You-Sheng et al. (Jan. 2014). "A generalized Reynolds analogy for compressible wall-bounded turbulent flows". en. In: *J. Fluid Mech.* 739, pp. 392–420. ISSN: 0022-1120, 1469-7645. DOI: 10.1017/jfm.2013.620.

Peltier, SJ et al. (2016). "Crosshatch roughness distortions on a hypersonic turbulent boundary layer". In: *Physics of Fluids* 28.4.

Yang, X.I.A et al. (2016). "Exponential roughness layer and analytical model for turbulent boundary layer flow over rectangular-prism roughness elements". en. In: *J. Fluid Mech.* 789, pp. 127–165. ISSN: 0022-1120, 1469-7645. DOI: 10.1017/jfm.2015.687.

Yang et al. (Feb. 2018). "Aerodynamic Heating in Wall-Modeled Large-Eddy Simulation of High-Speed Flows". en. In: *AIAA Journal* 56.2, pp. 731–742. ISSN: 0001-1452, 1533-385X. DOI: 10.2514/1.J056240.

Bernardini, Matteo et al. (2021). "STREAmS: A high-fidelity accelerated solver for direct numerical simulation of compressible turbulent flows". In: *Computer Physics Communications* 263. DOI: https://doi.org/10.1016/j.cpc.2021.107906.

Chung, Daniel et al. (Jan. 2021). "Predicting the Drag of Rough Surfaces". en. In: *Annu. Rev. Fluid Mech.* 53.1, pp. 439–471. ISSN: 0066-4189, 1545-4479. DOI: 10.1146/annurev-fluid-062520-115127.

Kocher, Brian et al. (June 2022). "Characterizing Streamwise Development of Surface Roughness Effects on a Supersonic Boundary Layer". In: *AIAA Journal* 60, pp. 1–14. DOI: 10.2514/1.J061623.

Kocher, Brian D et al. (2022). "Characterizing streamwise development of surface roughness effects on a supersonic boundary layer". In: *AIAA journal* 60.9, pp. 5136–5149.

Modesti, Davide et al. (July 2022). "Direct numerical simulation of supersonic turbulent flows over rough surfaces". en. In: *J. Fluid Mech.* 942, A44. ISSN: 0022-1120, 1469-7645. DOI: 10.1017/jfm.2022.393.

Hasan, Manzoor A. et al. (Feb. 2024). "Estimating Mean Profiles and Fluxes in High-Speed Turbulent Boundary Layers Using Inner/Outer-Layer Scalings". en. In: *AIAA Journal* 62.2, pp. 848–853. ISSN: 0001-1452, 1533-385X. DOI: 10.2514/1.J063335.

Miller, Mark A. et al. (May 2024). "Hexagonal roughness characterization in turbulent flow". en. In: *Exp Fluids* 65.5, p. 66. ISSN: 0723-4864, 1432-1114. DOI: 10.1007/s00348-024-03801-4.

Cogo, Michele et al. (Apr. 2025). "Surface roughness effects on subsonic and supersonic turbulent boundary layers". en. In: *J. Fluid Mech.* 1009, A56. ISSN: 0022-1120, 1469-7645. DOI: 10.1017/jfm.2024.1232.

C. Riassunto in italiano

Abstract

Capire il comportamento dei fluidi comprimibili che scorrono su superfici rugose è un aspetto fondamentale per svariate applicazioni in campo aerospaziale, specialmente quelle riguardanti i rientri atmosferici, i sistemi propulsivi, la missilistica e i velivoli ad alta velocità. Ogni superficie in realtà presenta delle asperità, anche se sembra apparentemente liscia ed è importante distinguere i casi in cui la topografia sia rilevante o meno nell'evoluzione fluidodinamica del flusso. L'influenza della rugosità è piuttosto ben nota nel regime incomprimibile e questa conoscenza getta le basi per una ulteriore elaborazione ed estensione delle teorie apprese al regime comprimibile; qui, infatti, gli effetti termodinamici come variazioni di densità e viscosità diventano importanti e vanno presi in considerazione. In aggiunta a ciò, fenomeni come onde d'urto e di espansione possono entrare in gioco. Per queste ragioni, è complicato predire il drag e lo scambio termico all'interno dello strato limite. I veicoli di rientro sono ricoperti da uno scudo ablativo che subisce un processo di pirolisi quando viene investito da un gas estremamente caldo. Durante la discesa, quindi si forma un pattern di rugosità sulla superficie dello scudo che interagisce con il flusso esterno, modificando le prestazioni aerodinamiche del veicolo. L'obiettivo di questa tesi è sviluppare un modello di parete che sia efficace nel descrivere i profili di velocità e temperatura all'interno dello strato limite, a partire da delle quantità note ad una certa distanza dalla parete (qui indicata come matching location) e da informazioni riguardanti la topografia della rugosità. Questo Lavoro si concentra sull'analisi di uno strato limite turbolento, adiabatico, a Mach $M_\infty = 2$ che scorre sopra degli elementi di forma cubica (i dati DNS di riferimento sono stati forniti da Cogo et al., 2025). Il modello sviluppato in questa tesi è un'estensione di quello ideato da Yang et al., 2016 per il regime incomprimibile, che è stato modificato per essere applicato ad un caso supersonico basandosi sul fatto che, vicino alla parete, gli effetti di comprimibilità del flusso sono trascurabili a causa del brusco rallentamento. Oltre le creste delle asperità invece, il profilo di velocità è determinato da una legge logaritmica. Per tenere conto delle variazioni di densità, è stata introdotta una trasformazione comprimibile (Van Driest, 1951), mentre il profilo di temperatura viene ricavato dall'analogia di Reynolds proposta da Zhang et al., 2014. I risultati del modello sono in accordo con i dati forniti dalle simulazioni DNS, sia per il caso di parete adiabatica che isoterma. In futuro potrebbe essere interessante analizzare geometrie più complesse e realistiche e comparare il modello con dati di simulazioni ipersoniche. Infine, sarà necessario accoppiare il modello ad una simulazione completa di una capsula durante la fase di discesa.

Introduzione

Negli ultimi anni, l'interesse verso tematiche come l'esplorazione spaziale e il trasporto commerciale ad alta velocità, ha conosciuto una notevole ripresa. Infatti, a causa dei recenti avanzamenti nella tecnologia dei materiali e dell'accesso allo spazio sempre più semplificato per le compagnie private, molti ricercatori si stanno impegnando a trovare nuove soluzioni per incrementare l'efficienza e l'affidabilità dei velivoli. Tut-

tavia, ci sono ancora molti aspetti che rappresentano delle barriere alla realizzazione di questi progetti: gli oggetti che volano ad altissime velocità attraverso mezzi fluidi devono sopportare resistenze aerodinamiche e temperature elevatissime. Conoscere accuratamente come i carichi meccanici e termici si distribuiscono intorno ai velivoli a causa dell'interazione con il flusso rappresenta un nodo cruciale nella definizione di nuove procedure di design più efficienti. Le complessità aumentano quando il flusso è turbolento e compressibile e la superficie è caratterizzata da una texture rugosa (dovuta ad esempio a fenomeni di erosione o a processi industriali). In particolare, è impossibile capire a priori (conoscendo solo informazioni sulla geometria) come la rugosità influisca sulle variabili di flusso. In aggiunta, fenomeni tipici dei flussi comprimibili (come onde d'urto e di espansione) possono causare variazioni improvvise del campo fluido. Per queste ragioni, è importante studiare inizialmente topografie semplici, con proprietà geometriche ben definite. Queste tematiche trovano applicazione in vari campi del settore aerospaziale:

- Le superfici aerodinamiche dei velivoli e dei missili sono soggette alla formazione di ghiaccio, con conseguente perdita della normale liscezza;
- I componenti dei sistemi propulsivi (come le palette delle turbine e gli ugelli) sono investiti da un fluido molto caldo e sono soggetti a fenomeni di degrado come erosione, pitting, corrosione e deposizione che compromettono l'integrità delle superfici;
- Infine, i veicoli di rientro sono ricoperti con da uno scudo ablativo che, durante la fase di discesa, genera un pattern rugoso più o meno regolare che è investito da un flusso ipersonico con conseguente formazione di onde d'urto.

Dato che la maggior parte degli studi effettuati sul tema riguardano il regime incomprimibile, che è stato già investigato estensivamente (Chung et al., 2021; Jiménez, 2004), non è ancora chiaro se lo stesso approccio è applicabile nel regime compressibile o meno (Bowersox, 2007). Il lavoro qui proposto è un'estensione del modello presentato da Yang et al., 2016 al regime compressibile. Esso tiene conto delle interazioni delle scie che si generano a valle degli elementi rugosi usando il concetto di "flow sheltering". Questo è un meccanismo che spiega come le scie generate dalle asperità possano comportarsi da "riparo" dal flusso esterno per gli elementi a valle.

Partendo dalle informazioni del flusso ad una certa distanza dalla parete, chiamata matching location, il modello restituisce i profili di velocità e temperatura nel log-layer. In questo modo è possibile predire i valori di drag per unità di area τ_w e calore scambiato q_w generati dalla superficie, senza risolvere interamente lo strato limite.

Setup

L'analisi usa come riferimento dei dati provenienti da simulazioni numeriche dirette (direct numerical simulations, DNS) di uno strato limite supersonico turbolento, effettuate ad un numero di Mach pari a $M_\infty = 2$, che scorre sopra degli elementi cubici allineati. Le simulazioni sono state svolte da Cogo et al., 2025 (fig. 38). Le simulazioni sono state molto dispendiose dal punto di vista computazionale e

sono state effettuate utilizzando STREAmS (Bernardini et al., 2021), un codice open source orientato alle moderne piattaforme per il calcolo computazionale ad alte prestazioni che fa uso di librerie per il calcolo parallelo. Il codice supporta architetture multi-GPU e risolve le equazioni di Navier-Stokes per un gas viscoso e termicamente conduttivo. Le risorse per una simulazione consistono in 256 GPU per una discretizzazione del dominio di sedici miliardi di nodi. Le simulazioni sono state computate dal cluster Leonardo presente al CINECA di Bologna.

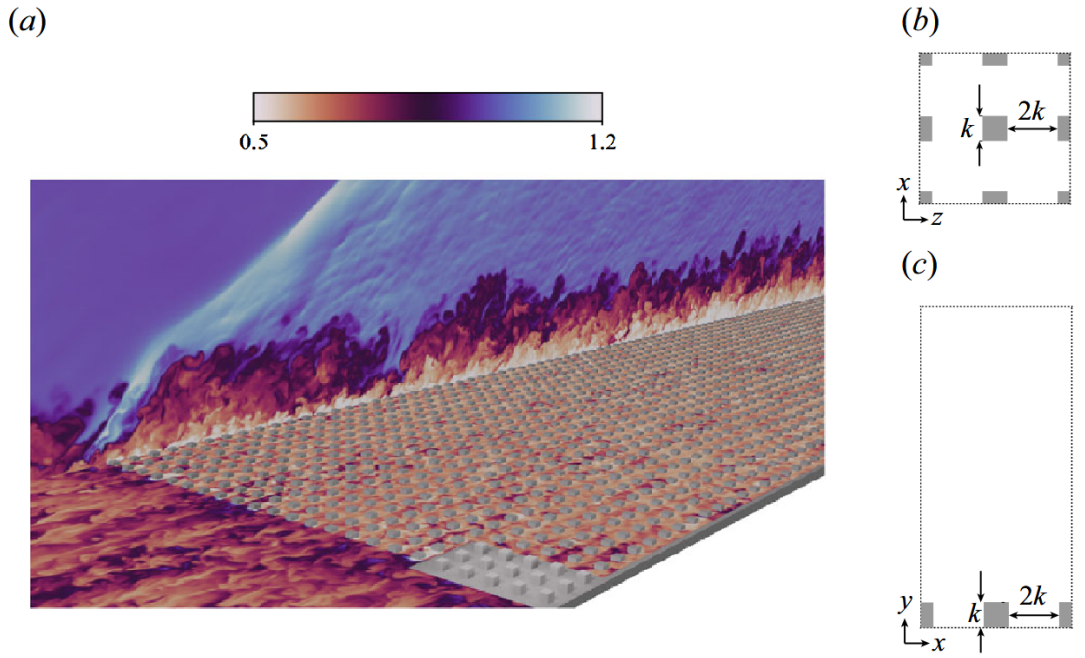

Figure 38: Campo di densità istantaneo ρ/ρ_∞ ricavato dai dati DNS usati come confronto in questo lavoro (Cogo et al., 2025

).

Modellazione della parete rugosa

Il modello qui presentato estende i concetti di quello sviluppato da Yang et al., 2016 al regime comprimibile. Esso assume che il profilo medio di velocità abbia una forma esponenziale al di sotto delle creste di rugosità:

$$\frac{U(y)}{U_h} = exp\left[a\frac{y-h}{h}\right] \tag{C.1}$$

dove $U(y)$ è la media spaziale/temporale della velocità del fluido, y è la coordinata in direzione normale alla parete, h rappresenta l'altezza degli elementi cubici e U_h è la velocità a $y = h$. Il coefficiente di attenuazione a dipende dalla densità e dalla distribuzione degli elementi rugosi ed è determinato usando il concetto di "flow sheltering". Per quanto riguarda il profilo logaritmico, il modello è stato differenziato e combinato con una trasformazione comprimibile (Van Driest, 1951) in

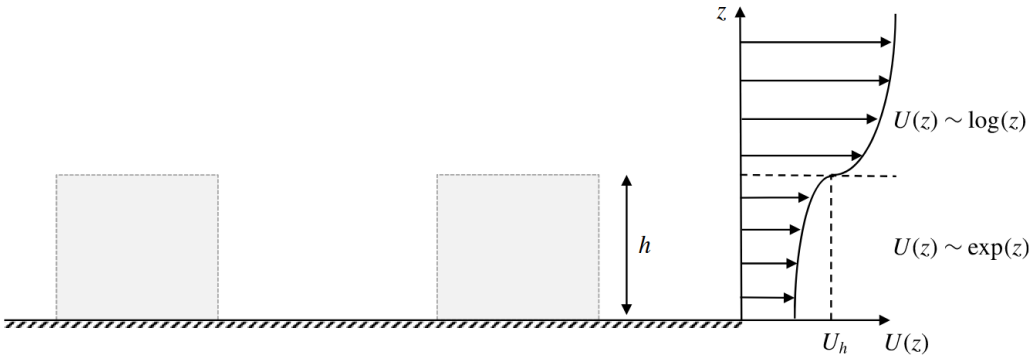

Figure 39: Profilo di velocità assunto nel modello: costituito da un layer esponenziale al di sotto delle creste di rugosità e da uno logaritmico al di sopra di esse, fino al bordo dello strato limite(Yang et al., 2016).

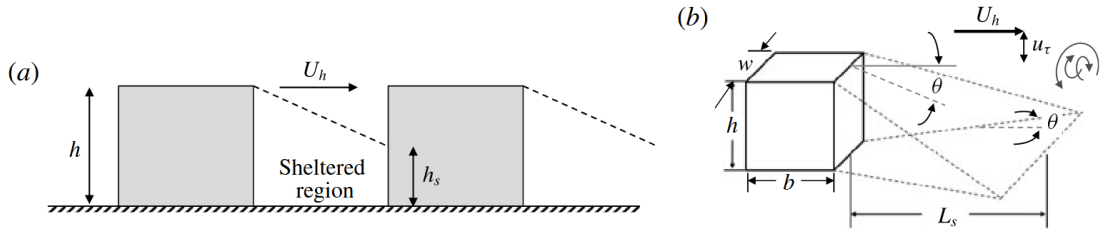

Figure 40: Concetto del meccanismo di "sheltering". (a) il flusso tra gli elementi è suddiviso in due regioni: una regione non riparata (unsheltered) con velocità caratteristica U_h e una regione riparata (sheltered) caratterizzata da una bassa quantità di moto. (b) Schema esemplificativo della scia a valle di un elemento cubico caratterizzata da una bassa quantità di moto (Yang et al., 2016).

modo da tener conto di possibili variazioni di densità dovute alla natura del fluido.

$$\frac{du}{dy} = \frac{u_\tau}{k}\frac{1}{y-d}\sqrt{\frac{\rho_w}{\rho}} \tag{C.2}$$

dove u_τ è la velocità d'attrito, k è la costante di Von Karman, d è l'origine virtuale del profilo logaritmico, e ρ è la densità. L'assunzione di base del modello è che gli effetti di comprimibilità sotto le creste degli elementi rugosi siano minimi poiché il flusso ha una bassa velocità e la densità si può considerare costante in questo substrato rugoso. Inoltre, si può notare che il profilo esponenziale non rispetta la condizione di aderenza, ma il suo ruolo è quello di fornire un valore della velocità ad altezza $y = h$ da cui far partire la legge logaritmica. Il profilo di temperatura medio invece è legato a quello di velocità nel log-layer tramite un'espansione in serie di Taylor al secondo ordine (Zhang et al., 2014):

$$T = b_0 + b_1 U + b_2 \frac{U^2}{2} \tag{C.3}$$

dove il coefficiente $b_0 = T_w$, mentre b_1 e b_2 sono ricavati dai valori di velocità e temperatura alla matching location e al bordo dello strato limite.

Procedimento di calcolo

Il procedimento per calcolare i profili di velocità e temperatura è il seguente:

- a partire da informazioni sulla topografia della rugosità, come l'altezza dei cubetti h e la solidità frontale λ_f (che è il rapporto tra l'area frontale di un cubetto e l'area totale del lotto in cui si trova) vengono estrapolati i parametri per descrivere l'intensità dello sheltering: il coefficiente di attenuazione a e il rapporto tra U_h e u_τ.
- I coefficienti b_0, b_1 e b_2 vengono determinati a partire dai valori noti di temperatura e velocità alla parete, alla matching location e al bordo dello strato limite.
- assumendo un valore iniziale di u_τ, il profilo esponenziale viene immediatamente calcolato, mentre quello logaritmico viene integrato a partire da $y = h$ fino alla matching location.
- la temperatura viene calcolata passo dopo passo usando l'equazione C.3 e la densità si ricava dalla legge dei gas ideali.
- se il valore della velocità alla fine dell'integrazione non coincide con quello della matching location scelta, il ciclo ricomincia con un nuovo valore di u_τ fino a convergenza.
- infine si calcolano il drag e lo scambio termico per unità di area.

Risultati

In questa sezione, il modello è messo a confronto con i dati di DNS forniti da Cogo et al., 2025. In figura 41, la velocità riscalata u^+ (rapporto tra velocità e velocità d'attrito) è mostrata in relazione alla coordinata normale alla parete, riscalata per la lunghezza viscosa δ_ν. Il modello estrapola correttamente le informazioni riguardanti la geometria della rugosità e come esse influiscano sulla dinamica del flusso. L'errore nella predizione del drag per unità di area è $\epsilon_{\tau_w} = 2.6\%$ per il caso di parete adiabatica e $\epsilon_{\tau_w} = 4.5\%$ per il caso di parete isoterma. Il profilo di temperature in figura 41 è in accordo con i dati di simulazione; quindi, il modello parabolico rappresenta una buona predizione. I grafici mostrano i risultati solo dall'altezza della rugosità alla matching location.

Conclusioni

L'obiettivo del modello presentato in questa tesi è di fornire uno strumento che possa predire l'evoluzione della dinamica del fluido lungo uno strato limite rugoso a velocità supersonica. Ciò permette di valutare gli effetti della scabrezza nelle variabili di flusso senza effettuare simulazioni molto dispendiose. Il modello proposto da Yang et al., 2016 è stato esteso nel regime comprimibile ed è stata implementata una trasformazione (Van Driest, 1951) nel layer logaritmico per tenere conto delle variazioni di densità. I risultati del modello concordano con i dati forniti dalle

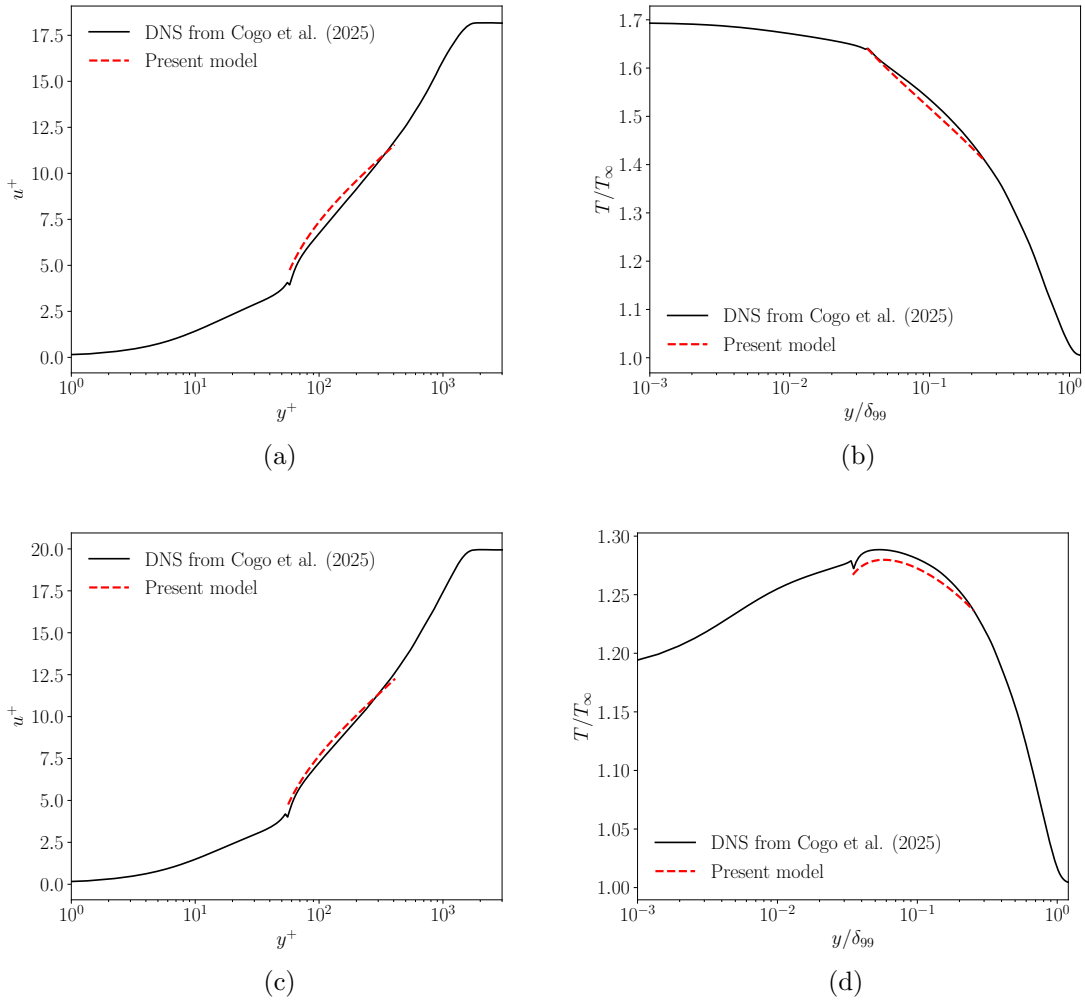

Figure 41: Profili di u^+ e T/T_∞ Cogo et al., 2025. Le curve sono mostrate solamente per il tratto che va dalle creste della rugosità alla matching location. (a) e (b) si riferiscono al caso di parete adiabatica $T_w/T_\infty \simeq 1.7$, mentre (c) e (d) a quello di parete isoterma $T_w/T_{aw} = 0.7$.

simulazioni: per il caso adiabatico l'errore nella predizione del drag per unità di area è di $\epsilon_{\tau_w} = 2.6\%$ mentre per il caso isotermo si ha $\epsilon_{\tau_w} = 4.5\%$ e $\epsilon_{q_w} = 3.4\%$. Il modello è stato testato anche su dati DNS riguardanti una superficie con elementi cubici sfalsati con risultati soddisfacenti. In future, verranno svolte altre prove su nuove geometrie e velocità ipersoniche appena i dati delle simulazioni saranno disponibili.